Original manuscript for: ***Journal of Fluid Mechanics, 1994, vol. 265, pp.65-95***

Experimental investigation of the flow field of an oscillating airfoil and estimation of lift from wake surveys

By
J. Panda[1] and K.B.M.Q. Zaman
NASA Lewis Research Center
Cleveland, OH 44135

Abstract

The flow field of an airfoil oscillated periodically over a reduced frequency range, $0 \le k \le 1.6$, is studied experimentally at chord Reynolds numbers of R_c = 22,000 and 44,000. For most of the data, the NACA0012 airfoil is pitched sinusoidally about one quarter chord between angles of attack (α) of 5° and 25°. The cyclic variation of the near wake flow field is documented through flow visualization and phase averaged vorticity measurements. In addition to the familiar dynamic stall vortex (DSV), an intense vortex of opposite sign is observed to originate from the trailing edge just when the DSV is shed. The two together take the shape of the cross section of a large `mushroom' while being convected away from the airfoil. The phase delay in the shedding of the DSV with increasing k, as observed by previous researchers, is documented for the full range of k. It is observed that the sum of the absolute values of all vorticity convected into the wake over a cycle is nearly constant and is independent of the reduced frequency and amplitude of oscillation but dependent on the mean α. The time varying component of the lift is estimated in a novel way from the shed vorticity flux. The analytical foundation of the method and the various approximations are discussed. The estimated lift hysteresis loops are found to be in reasonable agreement with available data from the literature as well as with limited force balance measurements. Comparison of the lift hysteresis loops with the corresponding vorticity fields clearly shows that the major features of the lift variation are directly linked to the evolution of the large scale vortical structures and the phase delay phenomenon.

1. Introduction

The phenomenon of dynamic stall on airfoils and lifting surfaces in unsteady flow environments has been studied experimentally and computationally for many years, both as an important practical problem and a challenging fundamental one as well. The phenomenon appears on helicopter rotor blades, rapidly maneuvering aircraft, fluttering compressor blades, wind turbines and even fish tails and insect wings. It is now well known that the unsteady fluid mechanics of an airfoil pitched above the static stall limit is characterized by the formation of a strong vortex on the suction surface, known as the dynamic stall vortex (abbreviated here as DSV), which is eventually shed into the wake. Presence of the DSV on the airfoil upper surface causes a dramatic increase in the airfoil lift which, however, decreases suddenly when the DSV is shed. Overviews of this dynamic stall phenomenon can be found in the papers by McCroskey (1982) and Carr (1985).

The flow field of an airfoil pitched periodically about a fixed axis is primarily influenced by the amplitude (α_a), the mean angle (α_{mean}) and the frequency of oscillation (f). Past studies on the subject indicate that the last parameter is the most influential. Non-dimensionalized as $k = \pi fc/U_\infty$, the `reduced frequency' represents the ratio of two time scales: one imposed by the pitching motion $1/(2\pi f)$, and the other by the free

[1] NRC resident research associate

stream velocity and the airfoil chord (conventionally half the chord is used), $c/2U_\infty$. Most of the previous experimental (e.g. Carr et al. 1977; Leishman 1990) and computational (e.g., Mehta 1978, Wu et al. 1987, Visbal and Shang 1988) studies on the phenomenon are confined to low values of k (<0.4). Small amplitude pitching motion at very high k has been studied by Koochesfahani (1987), among others, but the small amplitude (±4°) apparently precluded the possibility of dynamic stall. Low Reynolds number studies of an airfoil undergoing combined oscillating and translating motion by Ohmi et al. (1990, 1991) also covered a high range of k (0.63 - 6.3). At high k they observed vortex formation due primarily to airfoil oscillation rather than translation; the vortical structure in the wake was found to be dependent on both k and amplitude of oscillation. However, the experimental part of their study was limited to flow visualization only. Gad-el-Hak and Ho (1986) also covered a wide range of k (0.2 to 3.0); but the experiment, which involved an airfoil of small aspect ratio to study three-dimensional effects, was again limited to flow visualization only.

Most previous flow visualization studies focused on the formation and evolution of the DSV over the airfoil upper surface. In comparison, the structure of the downstream wake was addressed only in a few experiments. An understanding of the wake structure originating from the dynamic stall process is important for the analysis of more complex flows, e.g., in machinery involving rows of blades (Cumpsty 1989). Robinson et al. (1986) observed the formation of a `trailing edge vortex' and a `tandem structure' in the wake of an oscillating airfoil. Gad-el-Hak and Ho (1986) also observed the formation of additional vortices due to the motion of the trailing edge. They observed that the complex flow field of an oscillating airfoil results primarily due to the mutual induction between the DSV and the `trailing edge shedding vortex'. In addition to the DSV, Ohmi et al. (1991) also observed vortical structures forming near the trailing edge whose strength depended on the velocity of the trailing edge and hence on the location of the pitch axis. In the early stages of the present study it became quite clear that the `trailing edge vortex' (TEV) could be as intense as the DSV. However, the role of the TEV, in comparison to that of the DSV, in the dynamics of the wake as well as in the unsteady forces exerted on the airfoil had remained unclear.

The wealth of data from the NASA Ames experiments (McAlister et al. 1978, 1982; Carr 1977) primarily focused on the unsteady forces experienced by the airfoil. This is also the case with several other experiments providing quantitative data (e.g., Leishman 1990). In only a few experiments were attempts made to measure the flow field and its cyclic variation. The vorticity distribution in the wake was measured by Mathioulakis et al. (1985) and by Booth (1987), but the measurements were limited in scope. The periodic flow provides an excellent opportunity to apply the phase-averaging technique in order to map the flow field and its variation with the oscillation phase. Such data could be quite helpful in computational studies of the subject and provide further insight into the mechanisms of the complex flow under consideration.

The general issues brought forth in the foregoing provided the motivation for the present study. The experiment was initiated as a part of our continuing research on control of separated flows over airfoils and blades (Rice and Zaman 1987; Zaman, McKinzie and Rumsey 1989). The objective at this stage has been fundamental in scope, to advance the knowledge in the area, maintain in-house expertise, and aid in computational efforts. Initially, detailed phase-averaged flow field measurements and flow visualization were carried out for specific cases of airfoil oscillation. These results have been summarized in a conference paper (Panda and Zaman 1992). Only the highlights of these results are included here.

During the analysis of the wake vorticity data, it occurred to us that the unsteady lift on the airfoil can be estimated from the vorticity flux shed into the wake. A detailed discussion of the analytical foundation of the method and the various approximations involved is deferred to a later section in the text. In short, the idea follows from the principle that the lift force acting per unit length of a pair of parallel, counter-rotating vortices of circulation Γ and $-\Gamma$, separated by a distance x, is equal to the rate of change of the associated impulse (Von Karman and Burgers 1943; Bisplinghoff et al. 1955); force = $d/dt(\rho x \Gamma)$. For the steady flow,

the vortex pair is constituted by the `starting vortex system' and the `bound vortex' around the airfoil, and the above equation leads to the familiar Kutta-Joukowski theorem, $L = \rho U_\infty \Gamma$. For the unsteady case, the shed vortices of circulation $\delta\Gamma$ in time δt should, according to Kelvin's theorem, correspond to an equal and opposite change in the circulation ($-\delta\Gamma$) around the airfoil. By measuring $\delta\Gamma$ from the vorticity flux in the wake and an average convection velocity U_{conv} for the vortices, the change in the lift in time δt could then be estimated as $\delta L = \rho U_{conv} \delta\Gamma$. The measurement and the choice of U_{conv} are discussed later in the text. The lift variation over the oscillation cycle, and hence the lift hysteresis loop, was thus constructed. The method produced lift hysteresis loops that had remarkable similarities with previous measurements (McAlister et al. 1982).

The method was attractive because the lift was obtained entirely from the wake survey. Determination of the forces on an oscillating airfoil is not an easy task. Force balance measurements can suffer from interference from structural resonances and static pressure distribution measurements can suffer from spatial resolution and sensor response limitations.

Subsequently, the analytical foundation of the method was studied further. Alternate formulations, due to Theodorsen (1935) and in the format of the analysis of Wu (1981), were considered. There is also a `non-circulatory' component of the unsteady lift due to the inertia of the fluid moving with the oscillating airfoil, which was also considered following Theodorsen's analysis. The details of these are discussed in section 4. Unfortunately, due to experimental limitations, the lift hysteresis loops for the dynamic stall cases could not be measured directly for comparison. Only limited results could be obtained with a force balance for a case at a very low k, with $\alpha_{mean} = 0°$, which involved smaller amplitude force variation. The problem faced in this connection will be described in the text, but as will be shown, the lift variation obtained from the wake survey compared quite well with the direct measurement for this particular case.

The aspect of unsteady lift estimation from the wake survey constitutes a major part of the present paper. Obtaining the lift hysteresis loop from the vorticity data also provided a unique opportunity to relate the various aspects of the lift variation directly to the vortical structures. In the following, the experimental procedure is first described in section 2. The flow visualization data, obtained by smoke-wire and smoke injection techniques, are discussed in section 3.1. The phase-averaged, span wise component of vorticity $\langle\omega_z\rangle$ (x,y,t), measured without invoking the Taylor hypothesis, are discussed in section 3.2. Spatial distribution of $\langle\omega_z\rangle$ (x,y) for fixed t and fixed k, and temporal distribution of $\langle\omega_z\rangle$ (y,t) for fixed x and different k are presented. The latter data are used to estimate the lift hysteresis loops. Section 4 is devoted to the lift calculation procedures and results. The main conclusions are then enumerated in section 5.

2. Experimental Procedure

The experiments were carried out in a low speed wind tunnel, the details of which have been described elsewhere (Zaman, McKinzie and Rumsey 1989). A two-dimensional model of a NACA0012 airfoil with 10.2 cm chord and an aspect ratio of 7.5 were mounted horizontally at the center (mid-height) of the test section (figure 1a). The airfoil was supported at the two ends by two 0.635 cm diameter rods each of which passed through a pair of cylindrical bearings housed in the tunnel walls. The pitching mechanism essentially consisted of a crank and a connecting-rod, together with a flywheel, to oscillate a lever arm. The lever arm (not visible in figure 1a) oscillated an output shaft which in turn was connected to one of the airfoil support rods via a flexible coupling. The oscillation amplitude was adjusted by changing the crank radius, and the oscillation frequency was adjusted by varying the motor rpm. The entire pitching mechanism was installed in a steel frame which was structurally isolated from the tunnel and secured to the vibration isolated bed plate of the test cell.

The measurements were carried out using a crossed hot-wire probe. The probe could be traversed in the streamwise (x) direction through a longitudinal slot in the test section floor and up and down in y for a

given x, through an automated computer controlled traversing mechanism. The co-ordinates x and y are referenced to the airfoil trailing edge at 0° angle of attack (figure 1b). All measurements reported are for the x-y plane at the mid-span location. The assumption of two-dimensionality is implicit in the investigation; data documenting the two-dimensionality of the flow field have been presented by Panda and Zaman (1992). The maximum blockage to the flow occurring at $\alpha_{max} = 25°$ was 8.5%. The probe movement, data acquisition and analysis were done by a MicroVAX 3300 computer.

For all data presented, the airfoil was oscillated sinusoidally about the one quarter chord location. An optical pick-up mounted on the driving motor shaft was used to provide the reference signal for phase averaging. Experiments were conducted at chord Reynolds numbers $R_c = 22{,}000$ and 44,000. Experiments for $k \leq 0.4$ were typically done at the higher R_c and for higher k at the lower R_c. For most of the data the angle of attack was nominally varied as $\alpha = 15° + 10°\text{Sin}(2\pi t/T)$, where T (= 1/f) is the period of oscillation. Limited experiments were conducted for oscillation amplitudes (α_a) of 4.2°, 7.2° and 14.1° with $\alpha_{mean} \approx 15°$, and for $\alpha = 0° + 7.2°\text{Sin}(2\pi t/T)$. In the following, the suffix "u" is used to indicate upstroke when α is increasing and "d" is used to indicate down stroke when α is decreasing.

For the smoke-wire flow visualization technique, a 0.005 inch nichrome wire was placed vertically either upstream of the airfoil or just downstream of the trailing edge. A flash unit was used to illuminate the smoke streaks which were photographed using a 35mm camera. Control of the smoke-wire operation was not fine enough to produce photographs at desired values of α. For some earlier photographs a small rod, marked every .25 inch by white dots, was placed downstream of the trailing edge. The position of the airfoil trailing edge relative to the marker determined the approximate angle of attack. The direction of motion was inferred from reviewing a large ensemble of photographs. For later experiments the signal from a phototransistor, activated by the camera flash, was compared with the reference optical pick-up signal for determining α more accurately. Limited flow visualization was done using a smoke-injection technique. Cigar smoke was introduced through a small port on the pressure surface, 1/8th chord from the leading edge and 1/3rd span away from one end. Only a small amount of smoke was injected to avoid producing a smoke jet.

As stated before, direct measurement of forces on the oscillating airfoil turned out to be difficult. Static pressure distribution measurement was not attempted because pressure transducers small enough to be fitted in the airfoil model yet having the required sensitivity for the low velocity range of operation were unavailable. A force balance, using load cells (Zaman and McKinzie 1991), was used to measure steady lift variation with α. The same balance was tried in an effort to measure the unsteady forces for the oscillating cases. However, harmonic distortion of the output signal became a problem; typically a harmonic near the structural resonance would become large especially at higher oscillation frequency. That the structural resonance was being excited became obvious when the stiffness of the support system was changed; this would result in a different harmonic (of the oscillation frequency) to become more prominent. For the $\alpha_{mean} = 15°$ case, the force changes were large as the airfoil went in and out of stall and the harmonic distortion was severe even at very low values of f. With $\alpha_{mean} = 0°$ and smaller amplitude ($\alpha_a = 7.2°$), the distortion was deemed minimal below an oscillation frequency of about 1 Hz. For such a case the lift variation with α was measured and compared with the wake survey results as will be presented in section 4.2.

3. Experimental results

3.1 Flow visualization

Figure 2 shows a sequence of photographs at various phases of the oscillation cycle, for $k = 0.2$, $\alpha = 15°+10°\text{Sin}(2\pi ft)$ and $R_c = 44{,}000$. The flow is from left to right. The marker with white dots is visible near the trailing edge. Frames (a) to (f) show phases when the angle of attack (α) is increasing (upstroke) and frames (g) to (j) show phases when α is decreasing (down stroke). As α increases, a clockwise vortex forms

on the airfoil surface (frame d). This is the "dynamic stall vortex" as referred to by previous researchers. With further increase in α, the DSV moves towards the trailing edge. When it reaches the trailing edge, a counter-clockwise vortex starts to form near the trailing edge (frame f). This vortex becomes clearer in frame (g) and can be seen more clearly in figure 3. The `trailing edge vortex' (TEV) grows quickly beneath the DSV (frames f and g) and lifts the latter from the airfoil upper surface. The DSV and the TEV combine to form a structure whose cross section looks like a mushroom. The `mushroom' structure evolves, moves upward and increases in size as it convects downstream (Frames h, i and j). In frame (i), at about 2½ chords from the trailing edge, its transverse extent is already very large and measures about 3 chords. After the passage of the `mushroom' structure, frames (j) and (a) indicate the passage of a few smaller vortices before flow reattachment takes place.

Literature on the oscillating airfoil problem addresses the dynamic stall vortex in detail and points to it as the reason for high lift; however, the trailing edge vortex and the `mushroom' structure have remained relatively unnoticed. As stated in section 1, such structures were observed by only a few, e.g. Robinson et al. (1986). The intense TEV and the enormous `mushroom' structure, which occur periodically at the oscillation frequency, could be quite significant in blade vortex interaction and aerodynamic noise generation especially in configurations involving rows of blades.

Figure 3 shows photographs of the DSV and the TEV when the latter has just formed. The smoke-wire photographs of frames (a) and (b) are for R_c = 22,000 and the smoke injection photograph of frame (c) is for R_c = 44,000. In (a) only the outline of the two vortices can be seen when the smoke wire is located upstream. The TEV appears unambiguously in (b) when the smoke wire is located just downstream of the trailing edge. The strong reverse flow at this location, and instant, pulls the smoke upstream and the cores of the two vortices are thus marked. Frame (c) is obtained by smoke injection from a port 1/8th chord away from the leading edge. Although the smoke is injected on the pressure surface, the DSV on the suction surface entrains most of the smoke. By analyzing several photographs, it is found that during the formation of the DSV, the stagnation point is located on the pressure surface downstream of the smoke injection port. Therefore, the injected smoke wraps around the leading edge and marks the DSV. When the TEV matures, as is the case for figure 3(c), the stagnation point moves back towards the leading edge and some smoke travels along the pressure surface to mark the TEV.

The photographs of figure 3 demonstrate the formation of the TEV. It appears that when the DSV reaches the trailing edge, the associated low pressure rapidly pulls fluid with anti-clockwise vorticity from the pressure surface causing the formation of the TEV. While the DSV dwells on the suction surface over a large part of the oscillation cycle, the passage of the TEV takes place within a much smaller fraction of the cycle. It will be shown later that the formation of the TEV causes a large oscillation in the lower branch of the hysteresis loop of the Cl versus α variation. Although initially small in size, the TEV grows to a large vortex when shed into the wake. The TEV is thrust against the DSV as they move into the wake. The two together pull fluid from the lower side of the flow field and take the appearance of the `mushroom'.

Effect of reduced frequency: Flow visualization photographs for various k have been shown by Panda and Zaman (1992) and these will not be repeated here. These photographs show that at very low k (≤0.05) the DSV and the TEV are not clearly visible and the flow field appears to be in a quasi-steady state. Wake velocity spectra at such low k (in the cited reference) show the dominance of the bluff body shedding that would have occurred if the airfoil were held at the maximum angle of attack. As k is increased above 0.1, the unsteady effects become prominent and the DSV, the TEV and the `mushroom' structure become clear. At k = 0.2 the sequence of vortex formation is such that the DSV and the TEV leave the trailing edge together, and this is followed by the shedding of smaller vortices. As k is increased to about 0.4 a small clockwise vortex rolls up on the upper surface and is shed in the wake before the dynamic stall vortex, while other

smaller vortices are suppressed. McAlister and Carr (1979) observed this smaller vortex preceding the DSV and called it the "shear layer vortex".

With further increase in k, a significant difference in the wake structure becomes evident. Figure 4 shows visualization photographs for k = 0.8 and 1.6, each for three phases of the oscillation cycle. It can be seen that while the `mushroom' structure is still upright at k = 0.8, it appears upside down at k = 1.6. Relative locations of the various vortices for these two cases are sketched in figure 5. At the lower k, the DSV is shed before the TEV and both of them move upwards in positive y. On the other hand, at k = 1.6, the TEV is shed earlier than the DSV and the resulting `inverted mushroom' remains in the same horizontal plane containing the pitch axis.

An expected trend with increasing k is the decrease in the spacing (wavelength) of the vortices in the wake. For k = 0.2 the spacing is estimated to be more than 10 chords while for k = 1.6 it decreases to 1.5 to 2 chords. An interesting effect of varying k is the resulting phase delay in the shedding of the DSV. From photographs similar to those for k = 0.2 (figure 2), it is observed that the DSV starts to nucleate at about $\alpha = 8°$ during the upstroke. The time elapsed until the airfoil reaches $\alpha = 25°$ is enough in this case for the DSV to move to the trailing edge. However, when k is increased the time needed by the DSV to form, grow and move to the trailing edge becomes larger compared to the time taken by the airfoil to complete the upstroke. At k = 0.8 this time is equal to the oscillation period and thus the shedding occurs at the end of the down stroke. A further increase in k, to say 1.6, causes two DSVs, one that has started to grow at the leading edge and one left from the previous cycle near the trailing edge, to reside on the airfoil suction surface simultaneously. The latter is shed in the upstroke part of the cycle. The occurrence of multiple vortical structures on the suction surface at high k has also been observed by Ohmi et al. (1991).

Figure 6 shows a plot of the angles of attack and the phase ($2\pi ft$) at which the center of the DSV is approximately above the trailing edge before it is shed into the wake, for various k. The values of α and $2\pi ft$ are related by $\alpha = 15° + 10°\sin(2\pi ft)$. Each data point is an estimate from several photographs similar to those shown in figure 2. Within the uncertainty of the estimation, the variation appears to be nearly linear. The solid line represents data of McAlister et al. (1978) for the same oscillation condition but for a much higher Reynolds number (2.5×10^6). The latter data represent the instants when the suction peak near the leading edge collapses. Good agreement of these data with the present result, within the k-range covered, indicates that the phase delay phenomenon for comparable airfoils may be essentially independent of Reynolds number. That Reynolds number is of secondary importance has been noted by previous researchers, e. g. McCroskey (1982). It is noteworthy here that McAlister et al. also showed that leading edge modification, such as by use of a boundary layer trip, can significantly alter the phase delay characteristics. The delay in shedding of the DSV has a significant effect on the lift experienced by the airfoil at various k. This will be discussed later in section 4.

3.2 Flow field measurements

The axial and transverse velocity components, ensemble averaged over many oscillation cycles, were measured in the wake as well as on the suction side of the airfoil outside the region covered by the pitching motion. The signals from the crossed hot-wire probes and the reference optical pick-up signal (section 2) was stored in a digital computer. The data were acquired at several x-stations, and at each x-station for several transverse locations (y). These were post-processed to obtain the phase-averaged distributions of $\langle u \rangle$ and $\langle v \rangle$. Typically the averaging was done over 80 cycles. The span wise vorticity component was given by

$$\langle \omega_z \rangle (x, y, \tau) = \frac{\partial \langle v \rangle}{\partial x} - \frac{\partial \langle u \rangle}{\partial y}$$

which was non-dimensionalized as, $\langle \omega_z \rangle^* = \langle \omega_z \rangle c/U_\infty$.

The distributions of $<\omega_z>^*$ for six phases are shown in figure 7 for k = 0.2; the instantaneous values of α are indicated. For k = 0.2, the distance through which the flow structures convect downstream in a period of oscillation is much larger than that covered by the measurement domain. Hence, each frame shows the wake structure for a small fraction of the `wavelength'. The data acquisition rate was chosen such that the phase-averaged distributions were computed for 50 time steps per cycle. Data for six time steps, capturing the essential features of the vortical structures, are shown and further data including the corresponding <u>- and <v>-distributions can be found in the reference, Panda and Zaman (1992). Note that the phases for the different frames in figure 7 are not at equal intervals. The measurement domain was divided into two parts; one over the suction surface and one downstream in the wake. Since results from the two sets are patched together there is some mismatch at the interface. The mismatch is believed to be mainly due to a slight phase drift between the two sets of measurements.

During the initial part of the cycle, as α is increased, the measurement region is relatively quiet and large vortices are absent. The wake region is marked by clockwise vorticity above the trailing edge and counter-clockwise vorticity below it. As the angle of attack is increased above 8°, a small vortical region is observed to nucleate near the airfoil quarter chord and grows rapidly with accumulation of positive vorticity. The nucleation of this vortical region over the airfoil is accompanied by an interesting change in the wake vorticity distribution. The negative vorticity in the lower part of the wake remains as is but the positive vorticity in the upper part of the wake depletes dramatically (e.g., at α = 20.7°u). The positive vorticity, generated on the airfoil suction surface which otherwise would have shed into the wake, starts to accumulate leading to the formation of the dynamic stall vortex.

Increasing α above about 18° causes a large portion of the accumulated vorticity to move towards the trailing edge. This represents the dynamic stall vortex and is marked as V1 in figure 7. The shedding of the DSV, generation of the TEV (V2) and the `mushroom' structure, and the subsequent formation of the smaller vortices observed in the vorticity data match well with the sequence observed with the flow visualization pictures. It is interesting to note that each of the clockwise vortices (V1, V3, V5) is followed up by a counter-clockwise vortex (V2, V4, V6). Therefore, the wake contains a series of clockwise and counter-clockwise vortices the strongest pair is made of the DSV (V1) and the TEV (V2).

The streamwise convection velocity of the different vortices could be calculated from the detailed space-time vorticity data. This was done by tracking the centers of the individual vortices over successive time steps. The convection velocity, obtained thereby, was somewhat lower for the larger vortices and also when the vortices were closer to the airfoil. Based on these data an *average* streamwise convection velocity $U_{conv}/U_\infty = 0.6$ was determined for the case of figure 7. This value was cross-checked by measuring the phase velocity at the fundamental about the streamwise station x/c = 0.3. The value $U_{conv}/U_\infty = 0.6$ was also found to be representative even when k was varied for the oscillation case under consideration. However, it changed considerably with variation of α_a and α_{mean}. For example, $U_{conv}/U_\infty = 0.8$ was measured for the case $\alpha = 0° + 7.2\mathrm{Sin}(2\pi ft)$. These values of U_{conv} are used in the lift estimation procedure discussed in the next section.

As indicated before, a crossed hot-wire probe was used to measure the velocity components after going through a standard yaw calibration. There are some errors in these measurements, especially due to hot-wire rectification during instants of large flow angularity and flow reversal. There is no easy way to assess the errors accurately and the exact extent of the errors in <u> and <v> measurements have remained unknown. However, an idea about the magnitude of the errors can be obtained by checking continuity at each measurement point. The departure of the quantity $(\partial<u>/\partial x + \partial<v>/\partial y)$ from zero, representing the departure from satisfying continuity, can be considered to be an indicator of the error in the measurement. Figure 8 shows contours of this quantity corresponding to three phases of figure 7. The nondimensionalization and the contour levels are the same as in figure 7. As expected, the measurement

error is found to be the largest on the upper surface when the DSV forms and is accompanied by strong reverse flows. In the wake, sufficiently far away from the airfoil, however, the errors are clearly minimal. Only during the passage of the strong vortices (e.g., 23.6°d case), do some errors occur due to large flow angularity. These measurements in the wake can be compared with similar measurements for free jets, e.g. of Zaman and Hussain (1981). The measurement errors on the outer edges of a jet are large because there is no forward velocity in the ambient and the passage of the vortical structures invariably induce reverse flow. In comparison, even the lowest velocity in the center of the wake is a large fraction of U_∞ and thus the vortical structures seldom induce reverse flow (except very near the airfoil). The wake flow measurements are thus relatively free from hot-wire errors.

Two-dimensionality of the flow field was checked through velocity measurements at various span wise (z) stations for constant x and y; these data have been reported by Panda and Zaman (1992). The phase-averaged velocity traces are quite similar indicating a reasonable two-dimensionality of the flow field. Note that the aspect ratio of the wing was 7.5 and all measurements reported in this paper were done at midspan and close to the trailing edge.

Temporal distributions of $\langle\omega_z\rangle$: Since the vorticity measurement via the spatial data acquisition technique involved extensive time and effort, such measurements were performed for only one case as described in the preceding. In order to further study the effect of various parameters, measurements of $\langle\omega_z\rangle$ (y,t) were performed at a fixed x-station (x/c = 0.3, if not mentioned otherwise) covering a complete period of oscillation, $0 \le t/T \le 1$. The term $\partial\langle v\rangle/\partial x$ in the expression for $\langle\omega_z\rangle$ was evaluated by measuring $\langle v\rangle$ at three closely spaced x-stations with x/c = 0.3 being the middle one. Central differencing provided $\partial\langle v\rangle/\partial x(y,t)$ while the term $\partial\langle u\rangle/\partial y(y,t)$ was evaluated by least squares fitting of the $\langle u\rangle(y,t)$ profiles. (It is possible to simplify the measurements and obtain $\partial\langle v\rangle/\partial x$ via the Taylor hypothesis. This would involve measurement of $\langle v\rangle$ at only one x-station as a function of time, and calculation of $\partial\langle v\rangle/\partial x = -(1/U_{conv})\partial\langle v\rangle/\partial t$ which, of course, would provide only an estimate of $\partial\langle v\rangle/\partial x$; Zaman and Hussain 1981). Profiles of $\langle\omega_z\rangle$, obtained from the two gradients, were measured typically for 24 y-stations covering $-.75 \le y/c \le 1.0$. Non-uniform y-steps were used to provide adequate resolution in the center of the wake.

The $\langle\omega_z\rangle(y,t)$ data are later used to evaluate the unsteady lift. Figure 9 shows the $\langle\omega_z\rangle^*$ (y,t) distributions for the two cases described in the figure caption. For these two sets of data a detailed evaluation of the lift hysteresis loops will be performed, as will be elaborated shortly. Figure 9(b) represents a dynamic stall case, the subject of the paper, for k = 0.16. Figure 9(a) shows data for $\alpha_{mean} = 0°$ and $\alpha_a = 7.2°$, a case chosen for which force balance measurements could be performed so that the lift variation estimated from the vorticity data could be compared directly. For the latter case, because of the small mean angle and small amplitude of oscillation, the vorticity distribution shows only a mild undulation. In comparison, the variations are large and the vorticity is distributed in lumps for the dynamic stall case in figure 9(b). The temporal distributions appear quite different from the spatial distributions of figure 7 (the temporal distribution for k = 0.2, to be shown later, is not much different from that for k = 0.16). This is mainly due to different scaling of the abscissa. While only a fraction of the `wavelength' is captured in figure 7, figure 9(b) shows a full `wavelength'. Differences between the spatial and the temporal distributions are also expected because the flow at the measurement station is still evolving and is far from a case of `frozen flow' (Zaman and Hussain 1981). A scrutiny of the data of figure 9(b) identifies the DSV and the TEV. The former is the concentrated lump of positive vorticity between the points II and III; the latter is the concentrated negative vorticity between the points III and IV. The successive lumps of vorticity (on the right of the TEV) represent the vortices shed later. The measurement errors for these data were also estimated using the continuity equation as described earlier. The largest errors were of similar magnitude as shown in Figure 8 (in the wake) and occurred generally at the interface of the DSV and the TEV.

4. Estimation of unsteady lift from the vorticity data

4.1 Analysis

As stated in section 1, the unsteady lift, L(t) can be divided into two components; `non-circulatory' $L_{NC}(t)$ and `circulatory' $L_C(t)$ (Bisplinghoff et al. 1955). The former has been alternatively referred to as the `virtual mass effect' or the `acceleration reaction' term (Batchelor 1967). This is dependent on k and can be negligible at small values of k. The latter component is, of course, due to the vortical flow arising from the airfoil surface.

Non-circulatory part: Theodorsen (1935) provided an analysis for this component of the lift for pitching as well as plunging motion of a flat plate based on the solution of the small disturbance potential equation (also see Bisplinghoff 1955). For pitching motion about the one-quarter chord point the expression reduces to

$$L_{NC}(t) = \rho \pi \frac{c^2}{4} (U_\infty \dot{\alpha} + \frac{c}{4} \ddot{\alpha}),$$

where $\dot{\alpha}$ and $\ddot{\alpha}$ are the angular velocity and acceleration, respectively. With

$$\alpha(t) = \alpha_{mean} + \alpha_a \, Sin\,(2 \pi f t)$$

the non-circulatory component of the lift coefficient becomes

$$Cl_{NC}(t) = \pi \alpha_a \,(k \, Cos\,(2 \pi f t) - \frac{k^2}{2} Sin\,(2 \pi f t)).$$

A few observations can be made from the above equation. First, Cl_{NC} increases with k, and becomes the dominant component at large k for a given flow condition. Second, Cl_{NC} is linearly dependent on the amplitude (α_a) but is independent of the mean angle (α_{mean}). Third, the net change of Cl_{NC} over a complete period of oscillation is zero. Finally, Cl_{NC} at a given α is different between the upstroke and the down stroke which yields a hysteresis loop in the Cl_{NC} versus α curve.

The decomposition of the total lift into the two components rests on linear assumptions allowing the superposition. When large vortices are present, and in the high k-range, nonlinear effects are expected. However, for small values of k, considered mainly in the present paper, the noncirculatory component can be negligible and the lift variation arises primarily due to the circulatory component.

Circulatory part: It is the circulatory component which is estimated from the vorticity flux in the wake. Let us begin with a brief review of the method to determine lift for a steady airfoil. If we consider an impulsively started flow over a fixed airfoil, a `starting vortex complex' is created which convects away from the airfoil. Once the steady state is reached, the net amount of vorticity shed into the wake over a finite time is zero and there is a constant circulation around the airfoil. This latter circulation associated with the `bound vortex', according to Kelvin's theorem, is equal and opposite to that of the `starting vortex complex'. As mentioned in section 1, the force acting per unit length of a pair of counter-rotating vortices of circulation $+\Gamma$ and $-\Gamma$ separated by a distance x is given by

$$\text{Force} = \frac{d}{dt}(\rho \times \Gamma).$$

For the steady airfoil, the `starting vortex complex' moves away from the airfoil at the free stream velocity, so that $dx/dt = U_\infty$, and this leads to the expression for the steady lift, $L = \rho U_\infty \Gamma$.

For the unsteady case of an oscillating airfoil, there is also a `starting vortex complex' shed before the periodic flow is established. However, the airfoil continues to shed an unbalanced positive or negative vorticity and the circulation of the `bound vortex' varies periodically with the oscillation. If within a finite time, δt, the circulation around all vortices shed into the wake is $-\delta\Gamma$, then by Kelvin's theorem this amount should be equal and opposite to the change in the circulation $\delta\Gamma$ of the `bound vortex' occurring within the same time. At any instant the shed vorticity in the wake with circulation $-\delta\Gamma$ and the corresponding change in the `bound vortex' $\delta\Gamma$, can be thought of as forming a counter-rotating vortex pair in which the vortices are moving away from each other at a convection velocity U_{conv}; U_{conv} is usually smaller than U_∞. Therefore, for the incompressible flow under consideration, the change in the lift in time δt can be estimated as

$$\delta L_c = \rho\, U_{conv}\, \delta\Gamma .$$

The change in the circulation $\delta\Gamma$ can be found by considering the fixed path ABCD, which encloses the airfoil, as shown in figure 1b. For a sufficiently large path, it is reasonable to assume that all vortical fluid is convected across the boundary CD only. For the two-dimensional, incompressible flow under consideration the time rate of change of circulation around the path ABCD is obtained, for example, from equation 5.25 of Potter and Foss (1982) as

$$\frac{d\Gamma}{dt} = -\int_{CD} u\, \omega_z\, dy + \int_{CD} \nu \left(\frac{\partial^2 u}{\partial x^2} + \frac{\partial^2 u}{\partial y^2} \right) dy .$$

By neglecting the contribution from the viscous term, which in the wake is smaller than the convection term by the order of the Reynolds number, one gets

$$\frac{d\Gamma}{dt} = -\int_{CD} u\, \omega_z\, dy .$$

Therefore, one can write

$$\frac{dL_c}{dt} = -\rho\, U_{conv} \int_{CD} u\, \omega_z\, dy .$$

Substituting $\xi_1(t) = \int_{CD} u\omega_z dy$ and integrating from time $t = 0$ one obtains

$$L_c(t) = -\rho\, U_{conv} \int_0^t \xi_1(t)\, dt + L_c(0) . \qquad \textbf{(1)}$$

The circulatory part of the lift at the beginning of the integration $L_c(0)$ represents a constant contribution towards the total lift from all vortices shed before time $t = 0$. This quantity cannot be

determined from the vorticity flux and is assumed to be zero. However, this is just an additive constant and the integration, carried through a period of oscillation, provides the change in the lift from its value at time t = 0; the shape of the lift hysteresis loop remains the same regardless of the starting point of integration.

A simplification in equation 1 is that it neglects the effect of the distribution of vorticity around the airfoil (region ABCD, figure 1) to the unsteady lift. However, the 'bound vortex' is not fixed at a point; it is distributed over the airfoil surface. Such a distribution will also contribute, although by a small amount, to the unsteady lift. The simplification is necessary in a practically feasible lift estimation procedure as measurement of unsteady vorticity around the airfoil would be extremely difficult. Effect of this simplification will be further discussed in the following in connection with equations 2 and 3. A caveat in Equation 1 is in the original formulation $\delta L_c = \rho U_{conv} \delta\Gamma$. Making assumption that the unsteady forces are due to the interaction of the shed vortex and the corresponding change in the bound vortex, neglects the interaction of the former with the bound vortex itself as well as with all vortices in the wake including the `starting vortex complex'. However, the effects due to the interactions of the shed vortex with the latter two vortex systems would mostly cancel each other, and thus equation 1 could be a reasonable approximation. But the accuracy has remained unclear. Note also that the formulation is equivalent to the application of the Kutta-Joukowski theorem to find the differential lift from the differential circulation, albeit using the convection velocity U_{conv} instead of U_∞ in the theorem. Of course, the convection velocity in the present context is not a clearly defined quantity. As discussed before, U_{conv}, say for the DSV, varies with streamwise distance. The DSV moves slowly when it is near the trailing edge but accelerates farther downstream (Panda and Zaman 1992). Thus, the choice of a constant U_{conv} in equation 1 involves an averaging process.

Alternate analyses for the unsteady lift calculation were searched for in the literature. This effort led to equations 2 and 3, which are described in the following. It should be emphasized here that all of the analyses considered have simplifications and a foolproof method is not in sight. The exercise in the following involves application of equations 1-3 to a given set of $u\omega_z(y,t)$ data to obtain the lift hysteresis loops, which are then compared with one another and with other available data to assess the validity of each equation.

The second equation for $L_c(t)$ is based on the flutter analysis of Theodorsen (1935). In this analysis the lift force on an unsteady flat plate is calculated from the instantaneous spatial distribution of vorticity in the wake. The wake is considered as a vortex sheet of strength γ_w per unit streamwise distance and the resultant expression for lift, given by Bisplinghoff et al., 1955, can be written in the present notations as

$$L_c(t) = -\rho U_\infty \int_0^\infty \frac{x + \frac{c}{2}}{\sqrt{(x + \frac{c}{2})^2 - (\frac{c}{2})^2}} \gamma_w(x, t)\, dx \ .$$

For the present calculation the spatial vorticity distribution is obtained from the temporal data via Taylor's hypothesis yielding $\gamma_w dx = \int u\omega_z dy dt = \xi_1(t)dt$; where ξ_1 as before, is equal to the vorticity flux $\int u\omega_z dy$, which is a function of time. The free stream speed is replaced by the convection speed U_{conv} to account for the slower speed of the large vortices shed during large amplitude oscillation. The distribution of the wake vorticity at any instant consists of a combination of vortices shed during many prior complete cycles (-nT to 0) and a current partial cycle (0 to t). The integration is carried through the partial `wavelength' from the trailing edge (corresponding to time 0 to t) and then over ten additional complete `wavelengths' (corresponding to time -10T to 0). Increasing the number of complete wavelengths further did not make a significant difference in the result. With all these modification the above equation can be written as

$$L_c(t) = -\rho U_{conv} \int_{-10T}^{t} \frac{x + \frac{c}{2}}{\sqrt{(x + \frac{c}{2})^2 - (\frac{c}{2})^2}} \xi_l(t)\, dt + L_c(0), \qquad \textbf{(2)}$$

The spatial location x in equation 2 is obtained by applying Taylor's hypothesis a second time. As in equation 1, the term $L_c(0)$ represents the unknown, fixed contribution from all vortices (including the `starting vortex complex') in the wake which are not considered in the integral expression. The primary difference between equations 1 and 2 is the weighting factor inside the integral of the latter. The weighting factor is greater than unity close to the airfoil and quickly decreases to unity for x>c/2. According to Von Karman and Sears (1938), who also arrived at Theodorsen's equation starting with F = d/dt(ρxΓ), the weighting factor arises when the 'bound' vorticity distribution over the airfoil is also taken into account. The moment of this vorticity about the airfoil half chord position is non-zero. This makes additional contribution to the lift leading to the weighting factor. As discussed earlier, equation 1 does not take such a distribution into account (moment of the `bound vortex' about the half chord is assumed to be zero), which also explains the absence of the weighting factor in equation 1. One notes that the weighting factor can be expressed in a binomial series as

$$\frac{(x + \frac{c}{2})}{\sqrt{(x + \frac{c}{2})^2 - (\frac{c}{2})^2}} = 1 + \frac{1}{2}(\frac{c/2}{x + c/2})^2 - \frac{3}{4}(\frac{c/2}{x + c/2})^4 + ...$$

Thus the leading term in equation 2 becomes equivalent to equation 1 and the difference between the two lies in the contribution from the higher order terms. Another difference between equations 1 and 2 is the lower limit of integration. However, when the lower limit in equation 2 was changed to 0 from -10T, the difference in the result was negligible (the difference was found to be less than 1% for k = 0.16).

Equation 3 is adopted after Wu (1981). Starting with the Navier-Stokes equation Wu derived the expression for $L_c(t)$ as

$$L_C(t) = \rho \frac{d}{dt} \int\int x\, \omega_z\, dx\, dy$$

It states that the force in the y direction (lift) equals the rate of change of the x-moment of all the vorticity in the flow field. Note that the above equation is a generalized formulation of the relation, force = d/dt(ρxΓ), used to obtain equation 1.

The above equation is based on first principles. Thus, if the vorticity distribution over the entire flow field were known the forces could be calculated accurately. However, as stated before it would be practically impossible to measure all the vorticity especially around the oscillating airfoil. Thus, the following approximations are needed. The moment of the vorticity distributed over the airfoil, assumed to act at the mid-chord, is once again neglected. From the measured distribution of $\omega_z(y,t)$ at a given x, a spatial distribution is constructed by invoking the Taylor hypothesis, as was done for equation 2. The unsteady lift, assumed to be acting at mid-chord, is then approximated as

Similar to equation 2, the position x is obtained by applying Taylor's hypothesis a second time.

$$L_c(t) = -\rho \frac{d}{dt} \int_{-10T}^{t} (x + \frac{c}{2})\, \xi_l(t)\, dt + L_c(0)\ . \qquad \textbf{(3)}$$

Here it should be mentioned that Wu's formulation would also provide drag and pitching moment through the rate of change of the quantities $\iint x\omega_z dxdy$ and $\iint xy\omega_z dxdy$, respectively. Theodorsen's formulations as well as a variation of equation 1 would also enable estimation of pitching moment. In this paper, however, we have only covered estimation of the unsteady lift.

Method of calculation: Phase averaged axial velocity $\langle u \rangle$ and the span wise component of vorticity $\langle \omega_z \rangle$ are used to evaluate all of the above equations. With appropriate nondimensionalization, the full expression for the periodic variation of the lift coefficient Cl_c is approximated, say from equation 1, as

$$Cl_c(t) = -2\frac{U_{conv}}{c}T\int_0^{t^*}\int_{CD} \langle u \rangle^* \langle \omega_z \rangle^* dy^* dt^* \ .$$

The superscript, *, represents non-dimensionalized quantities (lift is nondimensionalized by $\frac{1}{2}\rho U_\infty^2 c$, $\langle \omega_z \rangle$ by U_∞/c, y by c and t by T). From the actual discrete measurements of $\langle \omega_z \rangle^*_{ij}$ and $\langle u \rangle^*_{ij}$ (where i = 1,NT and j = 1,NY; NT: number of intervals in a cycle and NY: number of y-steps) the above equation at any time step n+1, $1 \le n \le NT$, is evaluated as follows

$$Cl_c(n+1) = -2\frac{U_{conv}}{c}T\sum_{i=1}^{n}\sum_{j=1}^{NY} \langle u \rangle^*_{ij} \langle \omega_z \rangle^*_{ij} \Delta y^*_j \Delta t^*_i \ .$$

As stated before, $Cl_c(1)$ is assumed to be zero.

As discussed in connection with figure 8, the hot wire measurements in the immediate vicinity of the airfoil trailing edge are marked by errors due to occasional flow reversal. On the other hand, implicit in the estimation of lift from the unsteady wake survey is the assumption that the vorticity field has not evolved significantly by the distance of the measurement station. At a far downstream location, if the time variation of vorticity has changed through interaction and evolution, a wrong time history of the forces would be estimated. Also implicit in the method is the assumption of two-dimensionality in the flow. At a far downstream location three-dimensional effects would set in the flow. Thus the measurement station needs to be as close to the airfoil trailing edge as possible. The choice of measurement station is dictated by the conflicting requirements; it needs to be close to the trailing edge yet far enough downstream to avoid large hot-wire errors. Thus all $\omega_z(y,t)$ measurements are carried out at $x_{meas}/c = 0.3$. This, however, introduces a time lag between the instants of measurement and the corresponding `event' taking place over the airfoil. This time lag is estimated as, $-x_{meas}/U_{conv}$, and accounted for in the calculation of the lift variation.

`Closing error' and `absolute vorticity flux': An interesting condition arising from the requirement of finite lift on the airfoil is that the total change of lift over one complete period of oscillation should be zero. Therefore, the above calculation requires

$$\sum_{i=1}^{NT}\sum_{j=1}^{NY} \langle u \rangle^*_{ij} \langle \omega_z \rangle^*_{ij} \Delta y^*_j \Delta t^*_i = 0 \ .$$

Usually, due to measurement errors this condition is not satisfied. This leads to $Cl_c(1) \neq Cl_c(NT+1)$, i.e., an unclosed hysteresis loop. For brevity, the deviation of this sum from zero is distributed over the entire cycle and only the resulting closed loops are presented in this paper. The `closing error' expressed as

$$\%\text{error} = \frac{\sum_{i=1}^{NT}\sum_{j=1}^{NY} < u >^{*}_{ij} < \omega_Z >^{*}_{ij} \Delta y^{*}_{j} \Delta t^{*}_{i}}{\sum_{i=1}^{NT}\sum_{j=1}^{NY} | < u >^{*}_{ij} < \omega_z >^{*}_{ij} | \Delta y^{*}_{j} \Delta t^{*}_{i}} \text{ x100}$$

is listed in table 1 for all the measurements. The denominator of the above expression represents the sum of the absolute values of all vorticity shed in a cycle of oscillation. This is referred to as the `absolute vorticity flux' and is also listed in table 1 which will be discussed later in section 4.4.

4.2 Lift variation for $\alpha = 0° + 7.2° Sin2\pi ft$

The unsteady lift variation for this oscillation condition, at k = 0.028 (f = 0.57 Hz) and R_c = 44,000, was measured with a force balance and also estimated using the above mentioned calculation procedures. The force balance data are presented first followed by a comparative evaluation of the calculations.

Force balance data: The unsteady lift variation measured by the force balance is shown in figure 10. The very low value of k was chosen to minimize harmonic distortions of the load cell signal (section 2). The steady state lift variation, also measured by the same force balance is shown by the dashed line. The latter shows a kink around $\alpha = 0°$, which, as discussed in the following, is believed to be due to laminar separation at this low operating Reynolds number. Such departure from linear variation due to laminar separation has been observed by others (e.g., Mueller and Batill 1982).

The unsteady measurements show a hysteresis loop even at this low oscillation frequency. The variation in the upper and the lower branches of the loop bear similarities with the steady state lift variation. At first sight, the hystersis loop is unexpected, since the dynamic stall phenomenon should not appear when the airfoil is oscillated within its static stall limit (Carr 1985). However, it is believed that laminar separation is responsible for the hystersis loop in much the same way as for the kink in the steady lift variation. For the steady airfoil, the flow remains separated on both surfaces around $\alpha = 0°$ resulting in near zero lift (Mueller and Batill 1982; Zaman and McKinzie 1991). Only when the angle of attack is increased (or decreased) sufficiently, does the flow reattach on the upper (or lower) surface resulting in the increase (or decrease) in lift. For the case of oscillation, the extent of the laminar separation on a given surface of the airfoil presumably depends on the direction of motion. In other words, the extent of the separation at a given value of α on a given surface of the airfoil during upstroke is different from that occurring during down stroke. This apparently causes the observed hystersis loop in the Cl curve. It is noteworthy that the flow exhibits the hystersis and has not reached a quasi-steady state even at this low frequency of oscillation of 0.57 Hz.

Estimated lift variation: Figures 11(a)-(c) show the lift hysteresis loops constructed from the data of figure 9(a) using equations 1-3, respectively. The solid line represents the calculated circulatory part and in each figure this is plotted such that the mean Cl at $\alpha = 0°$ matches the corresponding steady state value of the Cl. The non-circulatory component is negligible at this low value of k. The lift curves obtained by all three equations exhibit hysteresis loops which are essentially similar and differences occur in the details. These loops are also very similar to the actual Cl variation of figure 10 and the maximum and minimum amplitudes are well represented. This reasonable agreement provides a validation of the lift

estimation technique, at least for the small amplitude of oscillation case. That the data for figures 10 and 11 are for the low Reynolds number case is incidental, and it is believed that the method should work just as well at high Re. It should be emphasized here that the data of figure 11 were very sensitive to small changes especially in oscillation frequency and in hot-wire calibration. This sensitivity could be partly attributed to the laminar separation which is known to be sensitive to the ambient conditions. Also the vorticity flux was small and thus accurate measurement was difficult; every time these data were retaken there was some difference in the lift hystersis loop. This could explain the differences between the estimated loops (Fig. 11) and the actual variation (Fig. 10).

4.3 Lift variation for k = 0.16, $\alpha = 15° + 10° Sin (2\pi ft - \pi/2)$

The circulatory component of the lift coefficient for k = 0.16 and R_c = 44,000 is shown in figure 12 (a)-(c) as given by equations 1-3, respectively. The data set of figure 9(b) is used for these results. Once again, the predictions are comparable and differences occur mainly where there are steep variations. For example, the magnitude of the large drop in the lift around 25° is predicted differently by the different equations. Since equation 3 involves differentiation, the resulting curve appears somewhat `jagged'. Unfortunately, there is no way to judge at this stage the relative accuracy of these finer differences. However, the fact that the predictions are similar for all three equations should be viewed as added confirmation that the overall features of the unsteady lift variation have been estimated successfully from the wake data. Of the three, equation 1 is perhaps the easiest to follow as it has similarity with the equation for steady lift calculation. In the following, further results on the unsteady lift variation for the dynamic stall case, obtained by using equation 1, are presented.

The circulatory component of Cl from figure 12(a) is added to the corresponding non-circulatory component (section 4.1) and the sum is shown in figure 13. The non-circulatory component is shown as the superimposed dashed curve which can be seen to be relatively small. The total unsteady Cl of figure 13 can now be compared with data from the literature. (As discussed before, the data in figure 13 show departure from the steady lift, and the Cl values are referenced to the value at $\alpha = 5°$ where it is assumed to be zero). Two sets of data for similar values of k are shown in figure 14. The data of McAlister et al. (1982), obtained by static pressure distribution measurement, are shown in figure 14(a). Figure 14(b) is included from a computational study by L. N. Sankar (private communication; see Wu, Huff and Sankar 1990), for conditions similar to that in figure 14(a). The overall features of the Cl variation in figure 13 can be seen to be similar to the data sets of figure 14. The slope of the upper branch (between I and II) and the small anti-clockwise loop around $\alpha = 25°$ (between III and IV) in figure 13 are in reasonable agreement with the data of figure 14(a). The main difference occurs in the lower branch of the loop. But some differences are not unexpected as the lift hysteresis loop is known to be sensitive to other flow parameters besides k, e.g. surface roughness, aspect ratio etc. The Reynolds number R_c was also quite different between the two experiments (4.4×10^4 in the present case as opposed to 4.8×10^5). The undulations on the lower branch, however, have been observed in other experiments (Leishman 1990), and can also be observed in the computational result shown in figure 14(b).

Lift hystersis loop vis-à-vis measured vorticity: The variations in the lower branch of the lift hysteresis loop, as discussed above, are believed to be real and due to the passage of the successive vortices following the DSV. In fact, the present way of estimating the lift provides a unique opportunity to relate various features of the hysteresis loop with the different vortical structures observed through the vorticity maps and the flow visualization. As discussed earlier, for the case under consideration, nearly all the positive (clockwise) vorticity generated from the airfoil suction surface accumulates to form the DSV

during the upstroke (between points I and II in figures 9b and 13). This is reflected in the wake as a depletion of positive vorticity. But the negative vorticity generated from the pressure surface is shed in the wake as usual. Qualitatively, a large negative vorticity in the wake is equivalent to a `starting vortex' and a large positive vorticity is equivalent to a `stopping vortex'. When the former is shed, circulation around the airfoil as well as lift increases, while shedding of the latter causes a drop in the lift. Thus, between points I and II the airfoil lift increases and between points II and III, when the DSV containing positive vorticity is shed, the lift drops. The rebounding of the lift near the highest angle of attack during the down stroke (III to IV) is due to the shedding of the trailing edge vortex which contains a concentration of negative vorticity. The undulations in the lower branch of the hysteresis loop occur due to the passage of a few more, relatively weaker positive and negative vortices following the DSV and the TEV (IV to I). Further comparison of the lift hystersis with corresponding $<\omega_z>^*$ data for other values of k are given in the next section.

4.4 Vorticity and lift hysteresis at different k and α_a

In order to study the parametric dependence of the dynamic stall and the corresponding lift hysteresis, the $<\omega_z>(y,t)$ distributions were measured and the lift hysteresis loops were computed for different values of reduced frequency k and amplitude α_a. Figure 15(a) shows vorticity data for various k similar to the data presented in figure 9.

The `closing error' and the `absolute vorticity flux' for the data of figures 9 and 15(a), as well as a few other sets not presented here, are tabulated in table 1. Referring back to section 4.2, recall that the closing error represents the difference between the first and the last point over a period in the computed Cl variation. This difference should be zero, which physically signifies the fact that the amounts of positive and negative vorticity convected into the wake over an oscillation cycle should be the same so that the net amount is zero. Due to measurement errors, however, the lift values computed from the $<\omega_z>^*$ data do not return to the original value at the end of the cycle resulting in the unclosed loop. It should be emphasized that this is a cumulative error integrated over the entire period for all the data. Thus, even though some of the numbers for the closing error in table 1 are in the double digits, in view of the complexity of the measurements, these should be considered as small.

An interesting observation can be made from the `absolute vorticity flux' data of table 1. This quantity represents twice the amount of the positive (or absolute negative) vorticity, shed into the wake over the period. It is seen to be approximately a constant (with appropriate nondimensionalization), and independent of k, R_c and α_a but dependent on α_{mean}. The size, shape and the sequence of formation of the various vortices vary depending on the oscillation parameters but the net amount of positive or negative vorticity carried by all such vortices in one oscillation cycle do not change significantly. Therefore, when the oscillation frequency and amplitude are changed, the vorticity generated from the airfoil surface is simply redistributed over the period. When α_{mean} is changed, however, the amount of positive or negative vorticity shed over the period is found to change considerably. This change occurs presumably because the mean pressure gradients near the leading edge and around the airfoil are changed when α_{mean} is changed. Since the pressure gradients are the primary source terms for the span wise component of vorticity (Reynolds and Carr 1985), the observed change in the vorticity generation is qualitatively accounted for.

The lift hysteresis loops corresponding to the $<\omega_z>^*$ data of figure 15(a) are shown in figure 15(b). Again, the solid lines represent the sum of both `circulatory' and `noncirculatory' parts while the dashed lines show the latter only. The Cl data can be discussed in comparison to the corresponding $<\omega_z>^*$ data. For the lowest k (= 0.05), the dynamic stall vortex is not well developed and the airfoil behaves in a

quasi-steady manner (Panda and Zaman, 1992). The $<\omega_z>^*$ data show a thick wake for most of the oscillation cycle indicating a stalled flow. The resulting lift hysteresis loop is also very small. The unsteady effects become prominent as k is increased above 0.1. Between k = 0.16 and 0.4 the main features of the $<\omega_z>^*$ distribution, viz. the thinner wake with stronger negative vorticity followed by the DSV and the TEV, are quite similar except for a progressive phase shift in the appearance of the vortices with increasing k. This is the same phase delay as discussed in section 3.1. At k = 0.16 (for which $<\omega_z>^*$ data are in figure 9b), the DSV and the TEV are shed before α_{max} (t/T > 0.5). This results in the small counter-clockwise loop at the lower right corner. At k = .2 the lift increases throughout the upstroke, dropping near α_{max} when the DSV is shed, and the resulting lift curve has only one large loop. As k is increased beyond 0.2, the lift keeps on increasing beyond α_{max} when the angle of attack is actually decreasing. For k $\approx$ 0.3 the sudden drop in Cl, associated with the shedding of the DSV, appears in the middle of the down stroke. Therefore the k = 0.3 and 0.4 cases show a second loop around α_{max}. A very similar sequence of change in the appearance of the lift hysteresis curve was also measured by Carr et al. (1977), in the range $0.1<k<.25$, from static pressure distribution data. However, the present data, allowing direct comparison of the lift variation with the vortices in the flow field, make it amply clear that the observed changes in the lift hysteresis are mainly due to the phase delay in the appearance of various vortices as k is increased.

With increasing k, the sequence of events becomes more complex. The $<\omega_z>^*$ distributions appear progressively different. At k = 0.8 multiple pairs of vortices are found to be distributed over the entire period. The resulting Cl versus α curve for k = 0.8 exhibits three loops. The noncirculatory component, shown by the dashed curves in figure 15(b), can be seen to grow in amplitude with increasing k and becomes the dominant contributor to the unsteady lift for k values above about 0.8.

Finally, in figure 16 a set of data are presented for varying amplitudes of oscillation with $\alpha_{mean} \approx 15°$. The corresponding $<\omega_z>^*$ data are not shown for brevity, but some of the corresponding features are listed in table 1. Data for k = 0.2 and 0.4 are shown for two amplitudes each. Corresponding data for the intermediate amplitude have been shown in figure 15. It becomes clear that the overall shapes of the hysteresis loops remain similar, only the size of the loop increases with an increase of amplitude. This is in general agreement with the data of Leishman (1990). However, Ohmi et al. (1990) observed that at very high k the effect of increasing α_a was equivalent to a decrease in k and vice versa. For the present data, the variation in the Cl loop for the four cases of figure 16 agrees with the sequence of events seen in the vorticity data. Limited flow visualization also indicated that the sequence of DSV and TEV and the phase delay in their shedding remain essentially unaltered with varying amplitude for a given k.

5. Concluding remarks

The significant observations and conclusions of the present study are enumerated in the following.

(1) In addition to the well known dynamic stall vortex (DSV) formed near the leading edge, an intense vortex of opposite sense is observed to form near the trailing edge (TEV) just when the DSV is shed. The combined DSV and TEV grow to a very large size and take the shape similar to the cross section of a `mushroom' as they convect away from the airfoil. For values of k in the range 0.2 - 0.4, the transverse extent of the `mushroom' structure measures about three chords just three chords downstream of the trailing edge. At large k the flow fields are complex, for example, at k = 1.6, the `mushroom' structure becomes inverted and two DSV's are observed to reside over the suction surface during part of the oscillation cycle.

The phase delay in the shedding of the DSV is found to vary approximately linearly with varying k over the full range of k covered in the experiment.

(2) The flow field is documented in detail using the phase averaging technique. The measured

evolution of the vorticity field over a cycle agrees well with the flow visualization photographs.

It is observed that the sum of either all clockwise or all counter-clockwise vorticity convected into the wake over a cycle is nearly constant and is independent of the reduced frequency and amplitude of oscillation but dependent on α_{mean}. As expected, the sum of all vorticity shed over the cycle is found to be nearly zero.

(3) A new method of estimating the unsteady component of lift from the vorticity flux measured in the wake is presented. The `circulatory' component of the lift is estimated as L_c = density x U_{conv} x cumulative vorticity flux shed by the airfoil from the beginning of an oscillation period, where U_{conv} is an average convection velocity. The analytical foundation of this method is discussed and alternate equations with different approximations are considered. The `non-circulatory' component is determined using Theodorsen's analysis. It is found that the estimated lift hysteresis loops compare well with limited force balance data for small oscillation amplitude with $\alpha_{mean} = 0°$. Direct comparison was not possible for the dynamic stall case, but the estimated lift variation showed reasonable agreement with data from the literature. Assumptions of two-dimensionality of the flow and insignificant evolution of the vorticity field are implicit in the estimation. From both of these considerations the measurement station should be as close to the airfoil trailing edge as possible. Possible application of this method to three-dimensional flow will require more research. However, even if approximate the method is a novel one and could be of interest in similar experiments in the future as the lift hysteresis loop is obtained strictly from wake surveys without direct force or static pressure distribution measurements.

(4) By comparing various features of the lift hysteresis loop with the corresponding vorticity fields and the flow visualization photographs, the following observations are made for a low k case: (a) The large lift occurring during the formation of the DSV is associated with an accumulation of positive vorticity on the airfoil upper surface and a depletion of the same in the wake. (b) As observed by previous investigators, the sudden drop in the lift occurs when the DSV leaves the airfoil surface. (c) The rebounding of the lift following the sudden drop is caused by the passage of the TEV. (d) Small oscillations seen in the lower branch of the hysteresis loop, also observed in a computational study cited in the text, are due to the generation and shedding of several smaller vortices following the DSV and the TEV.

(5) Hysteresis loops in the Cl vs. α curve are constructed for several values of the reduced frequency in the range $0.05 \leq k \leq 1.6$ using the method based on the wake survey. It is found that certain major features of the lift hysteresis at various k can be linked to the phase delay in the shedding of the DSV. For $k < 0.2$ the DSV is shed before α_{max} is reached causing a small counter-clockwise loop at the lower right corner of the larger clockwise loop. At $k = 0.2$ the lift increases throughout the upstroke until the DSV is shed around α_{max} resulting in a lift curve that has a single clockwise loop. For larger values of k the lift keeps on increasing beyond α_{max}, as the shedding of the DSV is delayed, resulting in a second counter-clockwise loop at the top right corner. With a further increase in k the hysteresis loops become increasingly more complex due to the multiple vortical structures involved in those cases.

While the `non-circulatory' component is small and negligible at low k, it becomes progressively larger with increasing k and for the case studied becomes the dominant one for $k > 1$.

Varying the amplitude of oscillation for a given k did not change the shape of the hysteresis loop, only the size varied proportionate to the amplitude.

Acknowledgement

The authors would like to acknowledge helpful comments from Dr. L. W. Carr, Dr. J. E. Bridges, Professors J.F. Foss, Y. Krothapalli and L. Van Dommelen during the course of this work.

REFERENCE

Batchelor, G. K. 1967 *An introduction to fluid dynamics*. Cambridge Univ. Press.

Bisplinghoff, R.L., Ashley, H. and Halfman, R.L., 1955, *Aeroelasticity*, Addison-Wesley.

Booth, E. R. 1987 Measurement of velocity and vorticity fields in the wake of an airfoil in periodic pitching motion. *NASA TP 2780*.

Carr, L. W. 1985 Dynamic stall - Progress in analysis and prediction. *AIAA Paper no. 85-1769-CP*, AIAA Atmospheric Flight Mechanics Conference.

Carr, L. W., McAlister, K. W. and McCroskey, W. J. 1977 Analysis of the development of dynamic stall based on oscillating airfoil experiments. *NASA TN D-8382*.

Cumpsty, N. A. 1989 *Compressor aerodynamics*, Longman Scientific and Technical.

Gad-el-Hak, M. and Ho, C-M. 1986 Unsteady vortical flow around three-dimensional lifting surfaces. *AIAA J.* **24**, no. 5, 713-721.

Koochesfahani, M. M. 1987 Vortical patterns in the wake of an oscillating airfoil. *AIAA paper 87-0111.*

Leishman, J.G. 1990 Dynamic stall experiments on the NACA 23012 aerofoil. *Experiments in Fluids*, **9**, 49-58.

McAlister, K.W. and Carr, L.W. 1979 Water tunnel visualization of dynamic stall. *J. Fluids Eng.* ASME transactions, **106**, 376-380.

McAlister, K.W., Carr, L.W. and McCroskey, W.J., 1978 Dynamic stall experiments on the NACA 0012 airfoil, *NASA TP 1100.*

McAlister, K.W., Pucci, S.L., McCroskey, W.L. and Carr, L.W., 1982 An experimental study of dynamic stall in advanced airfoil sections, vol. 2, pressure and force data, *NASA TM 84245*.

McCroskey, W. J. 1982 Unsteady Airfoils. *Annual Review of Fluid Mechanics,* **14**, 285-311.

Mehta, U. B. 1978 Dynamic stall of an oscillating airfoil. *AGARD CP-227, Paper 23*.

Methioulakis, D. S., Kim, M. J., Telionis, D. P. and Moor, D. T. 1985 On the wake of a pitching airfoil. *AIAA paper no. 85-1621*.

Muller, T. J. and Batill, S.M. 1982 Experimental studies of separation of a two-dimensional airfoil at low Reynolds numbers. *AIAA J.* **20**, 475-463.

Ohmi, K., Coutanceau, M., Ta Phouc Loc, and Dulieu, A. 1990 Vortex formation around an oscillating and translating airfoil at large incidences. *J. Fluid Mech.* **211**, 37-60.

Ohmi, K., Coutanceau, M., Daube, O. and Ta Phuoc Loc 1991 Further experiments on vortex formation around an oscillating and translating airfoil at large incidences. *J. Fluid Mech.* **225**, 607-630.

Panda, J. and Zaman, K.B.M.Q. 1992 Experimental investigation of the flowfield of an oscillating airfoil. *AIAA Paper 92-2622*.

Potter, M. C. and Foss, J. F. 1982 *Fluid Mechanics.* Great Lakes Press, Inc.

Reynolds, W. C. and Carr, L. W. 1985 Review of unsteady, driven, separated flows. *AIAA paper no. 85-0527*.

Rice, E. J. and Zaman, K. 1987 Control of shear flows by artificial excitation, *AIAA paper no. 87-2722*.

Robinson, M. C., Helin, H. E. and Luttges, M. W. 1986 Control of wake structure behind an airfoil. *AIAA paper 86-2282*.

Theodorsen, T. 1935 General theory of aerodynamic instability and the mechanism of flutter. *NACA report 496*.

Visbal, M. R. and Shang, J. S. 1988 Investigation of the flow structure around a rapidly pitching airfoil. *AIAA J.* **27**, no. 8.

Visbal, M. R. 1991 On the formation and control of the dynamic stall vortex on a pitching airfoil. *AIAA paper 91-0006*.

Von Karman, T. and Burgers, J.M. 1943 General aerodynamic theory of perfect fluids, in *Aerodynamic theory, vol. II* (Ed. W.F. Durand), Durand reprinting committee, Pasadena, calif.
Von Karmann, Th. and Sears, W.R., 1938, "Airfoil Theory for non-uniform motion", *J. Aeronautical Sciences, 5* (10), pp. 379-390.
Westphal, R.V. and Mehta, R.D. 1984 Crossed hot-wire data acquisition and reduction system. *NASA TM 85871*.
Wu, J. C. 1981 Theory of aerodynamic force and moments in viscous flows. *AIAA J.* **19**, no. 14, 432-441.
Wu, J.-C., Huff, D.L. and Sankar, L.N. 1990 Evaluation of three turbulence models in static air loads and dynamic stall predictions. *J. Aircraft*, vol. 27, 382-384.
Wu, J.-C., Kaza, K. R. V. and Sankar, L. N. 1987 A technique for the prediction of airfoil flutter characteristics in separated flow. *AIAA paper 87-0910*.
Zaman, K. B. M. Q. and Hussain, A. K. M. F. 1981 Taylor hypothesis and large-scale coherent structures. *J. Fluid Mech.* **112**, 379-396.
Zaman, K. B. M. Q. and McKinzie, D. J. 1991 Control of laminar separation over airfoils by acoustic excitation. *AIAA J.* **26**, no. 7, 1075-1083.
Zaman, K. B. M. Q., McKinzie, D. J. and Rumsey, C. L. 1989 A natural low-frequency oscillation of the flow over an airfoil near stalling condition. *J. Fluid Mech.* **202,** 403-442.

Table 1. `Closing error' and 'absolute vorticity flux' for different cases.

α	$R_c x10^{-3}$	k	%closing error	$\sum\sum \lvert <u>^*_{ij} <\omega_z>^*_{ij} \rvert$ absolute vorticity flux
	44	.05	-1.26	1.03
	44	.1	-4.03	.95
	44	.16	4.04	.94
15.3°±9.7°	44	.2	2.78	.93
	44	.4	1.83	.95
	22	.4	1.66	1.02
	22	.6	11.9	1.03
	22	.8	3.8	1.1
	22	1.2	3.8	1.0
	44	.2	13.3	.85
15.7°±7.2°				
	44	.4	9.1	1.07
	44	.2	8.5	.88
14.1°±14.1°				
	44	.4	15.7	1.04

	44	.036	7.9		.34
0°±7.2°					
	44	.028	1.6		.34

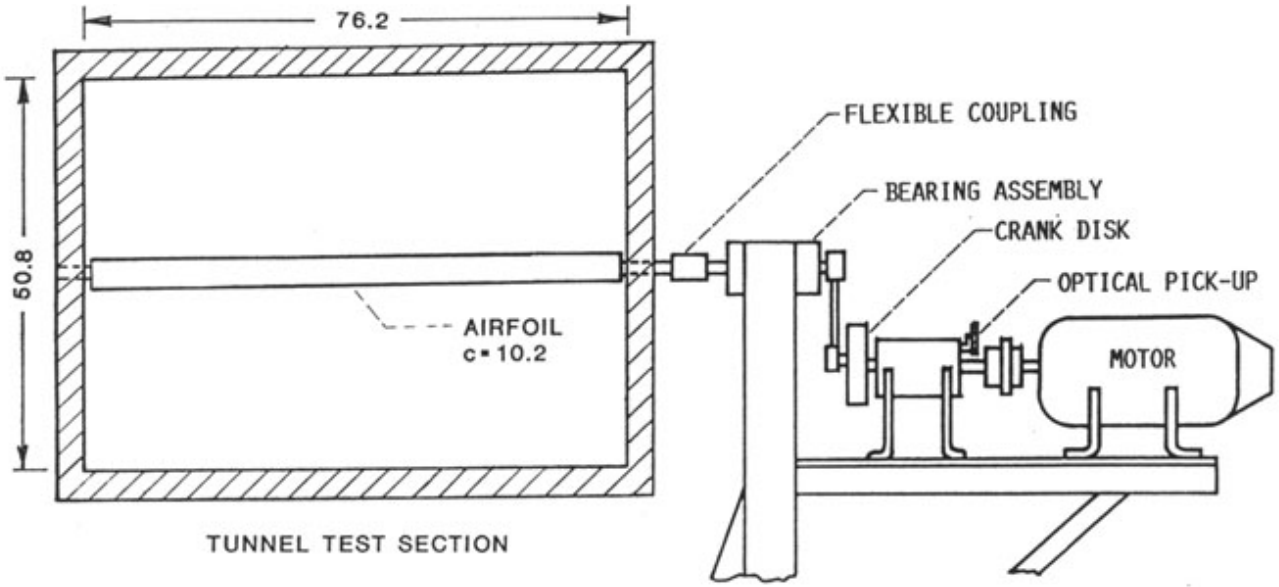

(a)

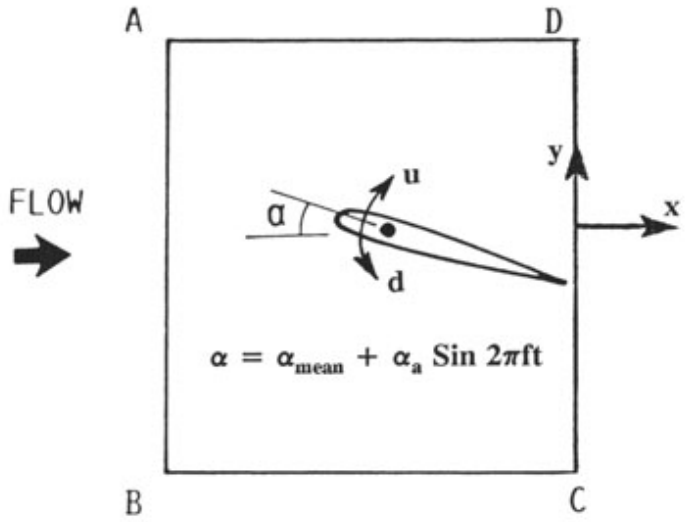

(b)

Fig. 1 (a) Schematic of wind tunnel test section and airfoil oscillation mechanism. (b) Coordinate system and control volume for calculation of unsteady circulation.

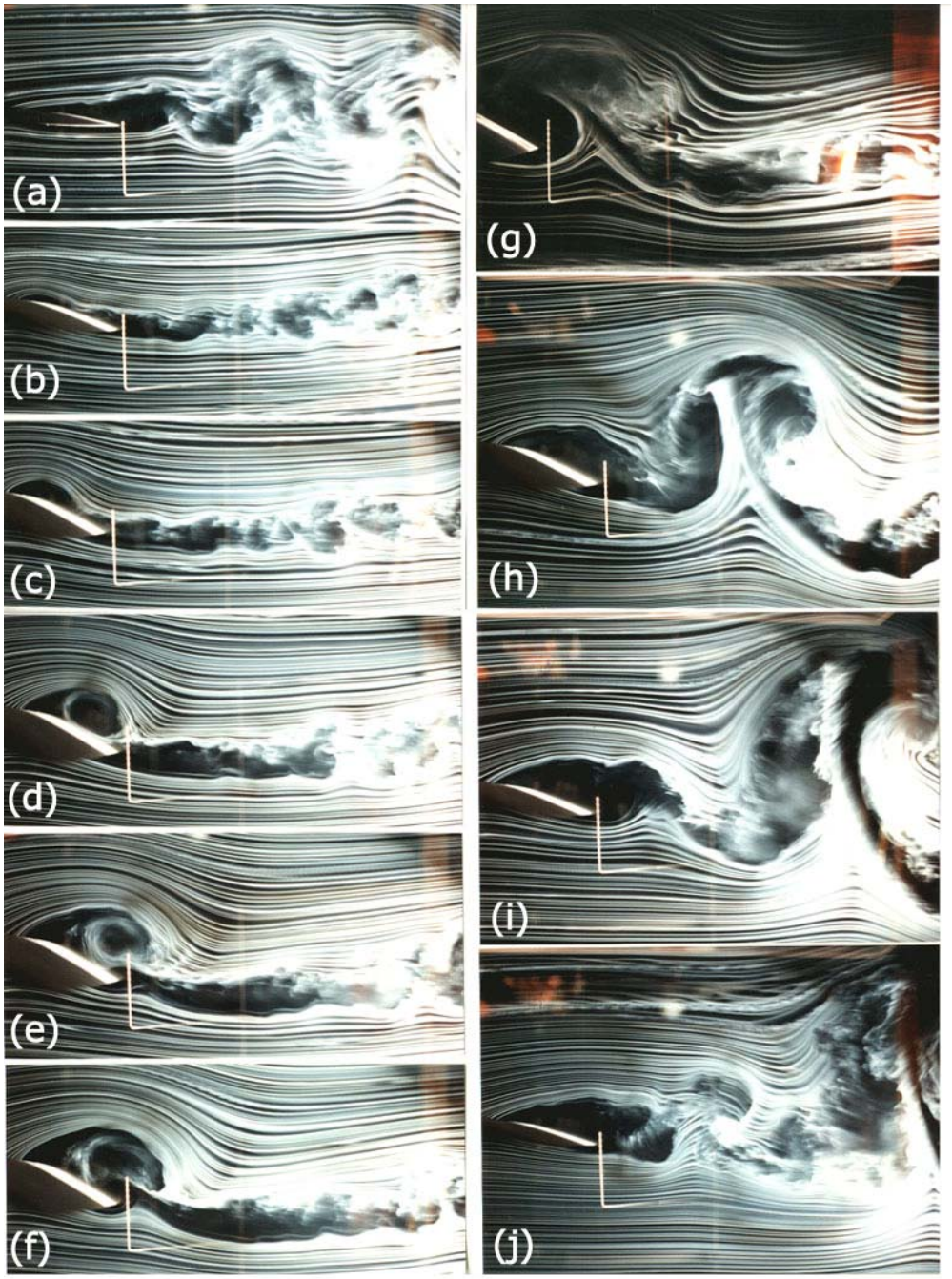

Fig. 2 Smoke-wire flow visualization photographs at different phases of the oscillation cycle; k = 0.2, α = 15°+ 10°sin2πft. Approximate α for pictures a to j are 5°u, 14°u, 20°u, 22°u, 24°u, 25°u, 25°d, 20°d, 16°d, 12°d; "u" and "d" denote increasing and decreasing α.

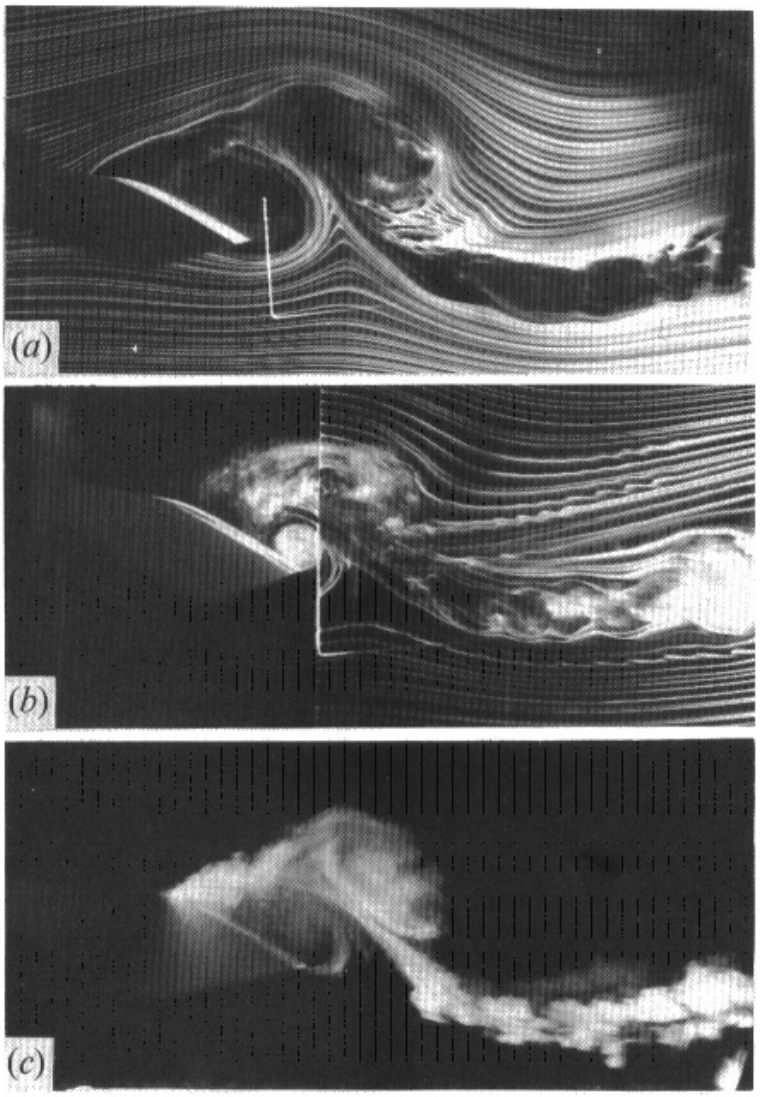

FIGURE 3. Flow-visualization photographs for the phase when the dynamic stall vortex and the trailing-edge vortex are shed into the wake ($\alpha \approx 25°$); $k = 0.2$, $\alpha = 15° + 10° \sin 2\pi ft$. (*a*) smoke wire placed upstream of airfoil leading edge, (*b*) smoke wire downstream of trailing edge, (*c*) smoke injection from a port on the airfoil lower surface.

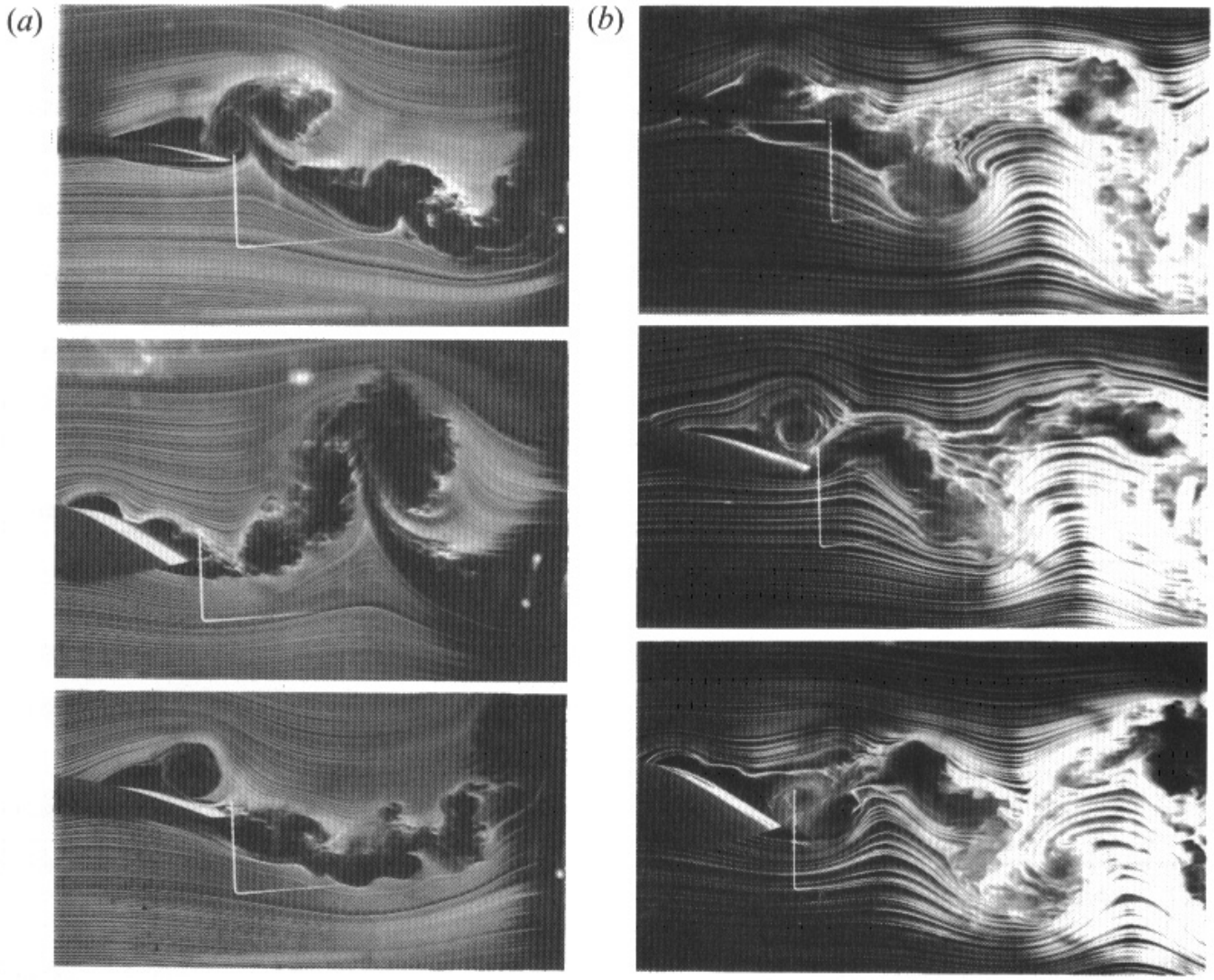

FIGURE 4. Smoke-wire flow visualization for two different k; $R_c = 22000$, $\alpha = 15° + 10° \sin 2\pi ft$. (*a*) $k = 0.8$; (*b*) $k = 1.6$. Approximate α from top to bottom for (*a*): 7°*u*, 23°*u*, 13.5°*d* and for (*b*): 5°, 15.5°*u*, and 25°.

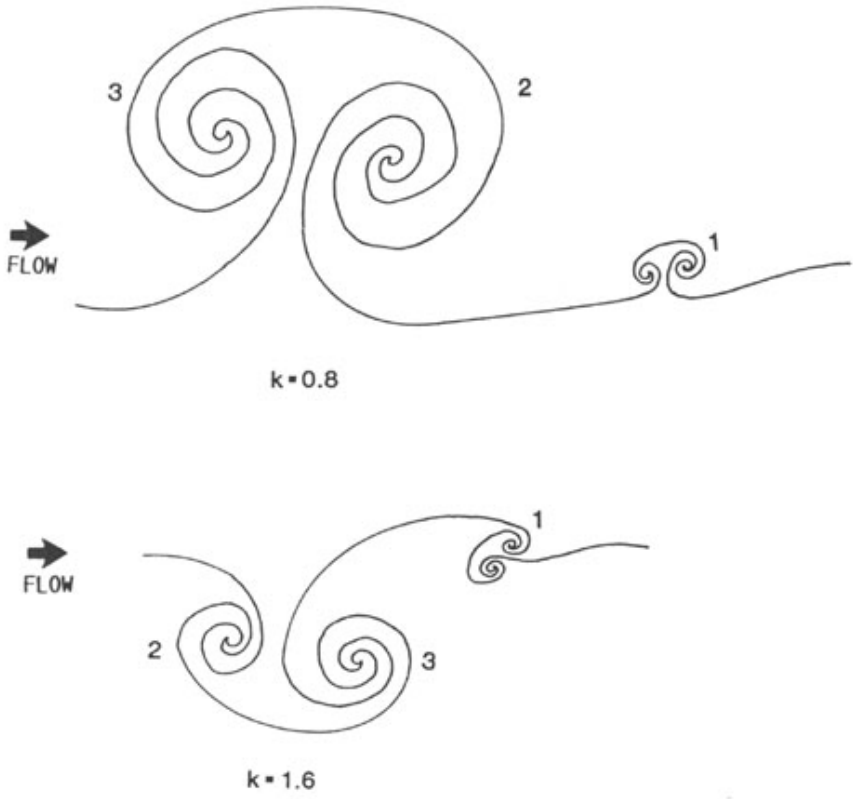

Fig. 5 Schematic of observed vortex structure in the wake for indicated values of k. 1: Shear-layer vortex, 2: Dynamic stall vortex, 3: Trailing edge vortex.

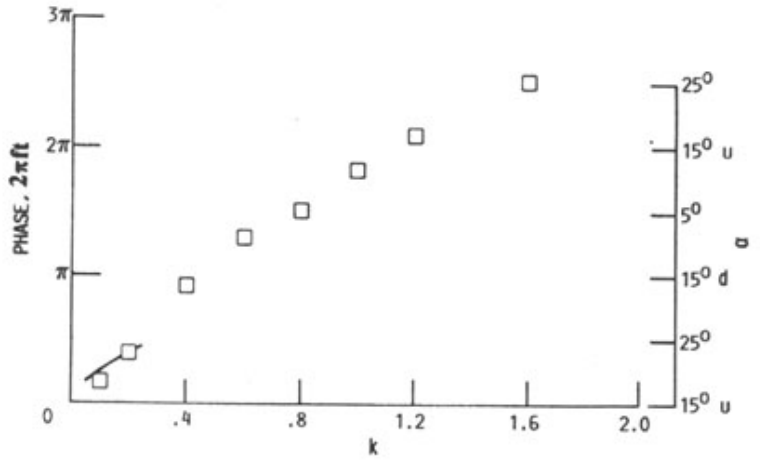

Fig. 6 Approximate phase when the center of the DSV is above the trailing edge, at different k. Solid line represents data of McAlister et al. (1978).

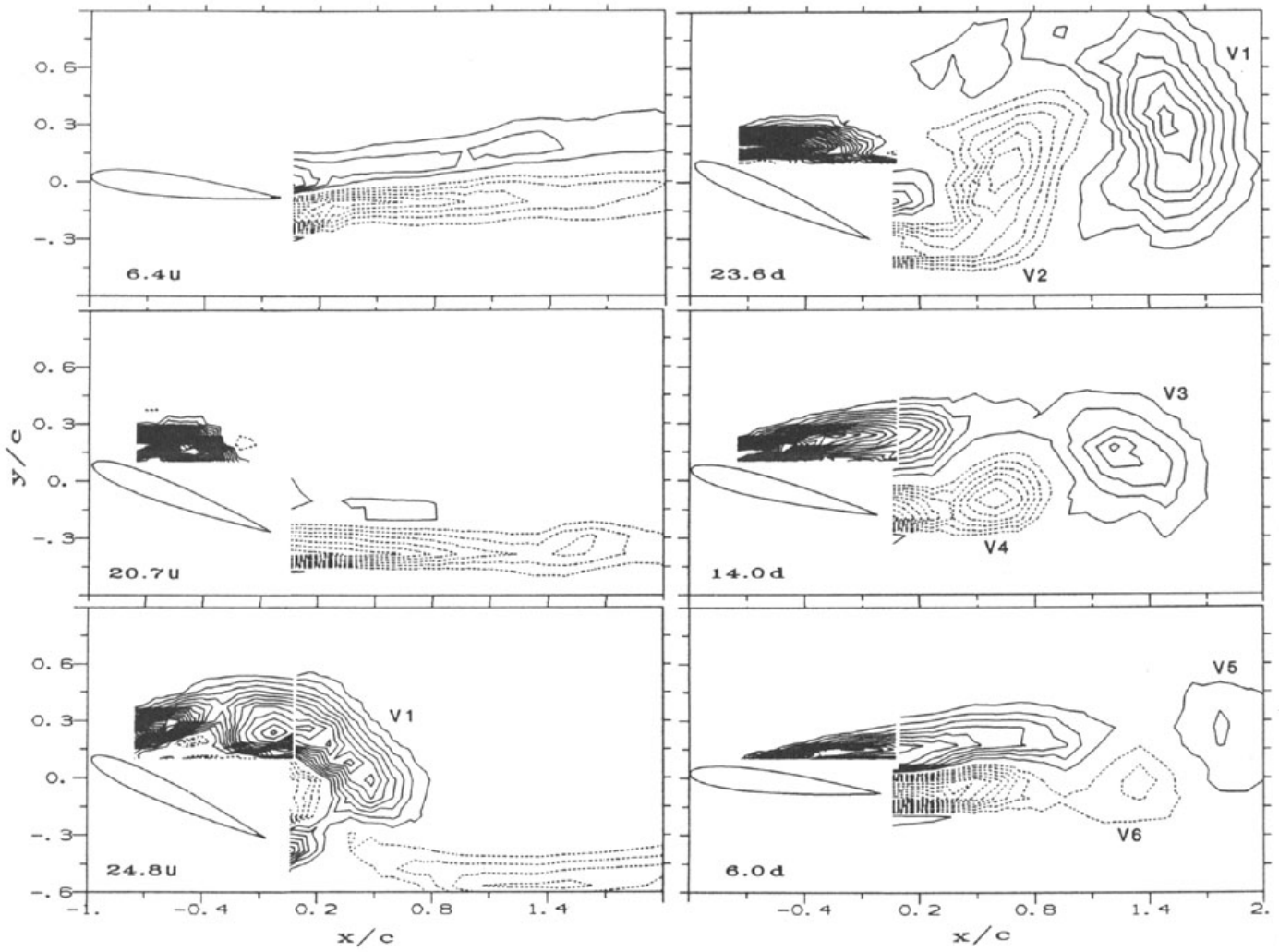

Fig. 7 Contours of spanwise vorticity ω_z, normalized by U_∞/c, for indicated α; k = 0.2, R_c = 44,000, $\alpha = 15° + 10°\sin 2\pi ft$. Contour levels for positive vorticity (solid line) start at 0.5 and for negative vorticity (dashed line) at -.5 and are at an interval of 0.5.

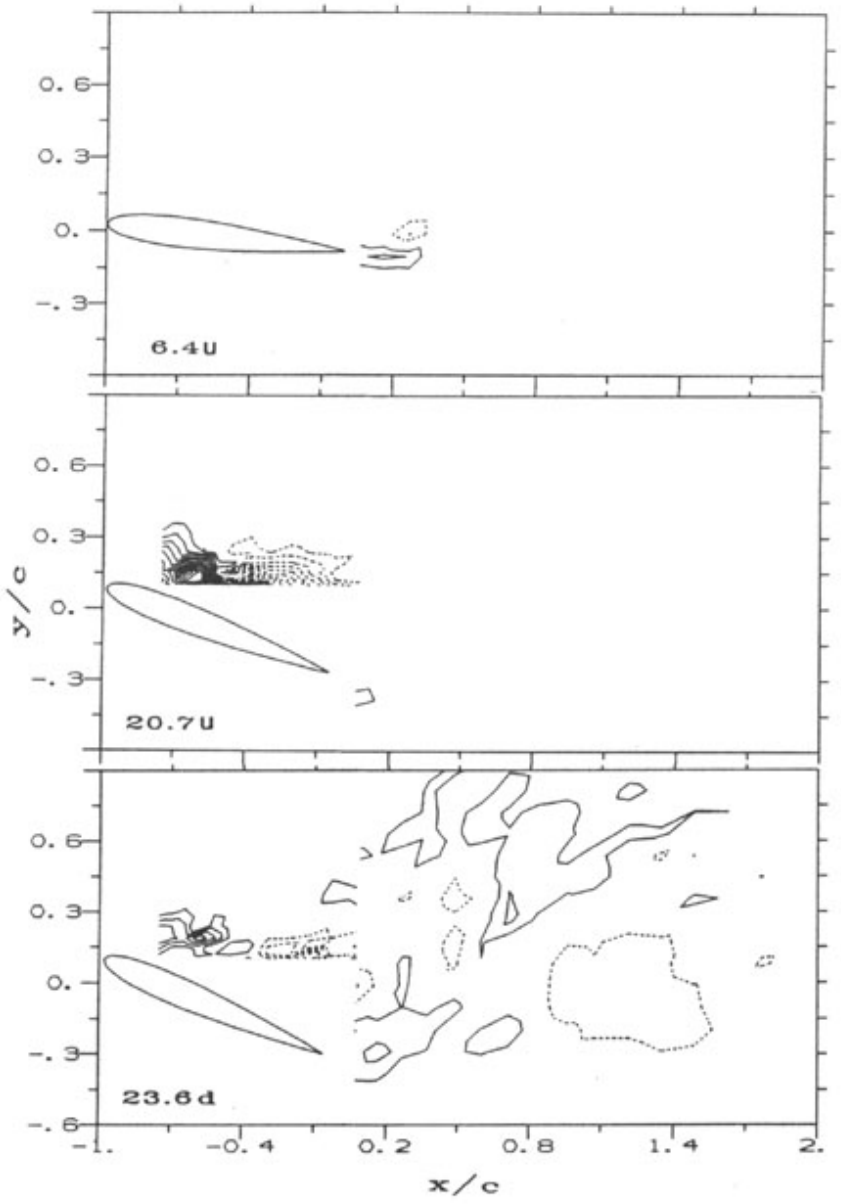

Fig. 8 Contours of $(\partial\langle u\rangle/\partial x + \partial\langle v\rangle/\partial y)$, normalized by U_∞/c, corresponding to the data of figure 7 for the indicated phases. Contour levels are same as in figure 7.

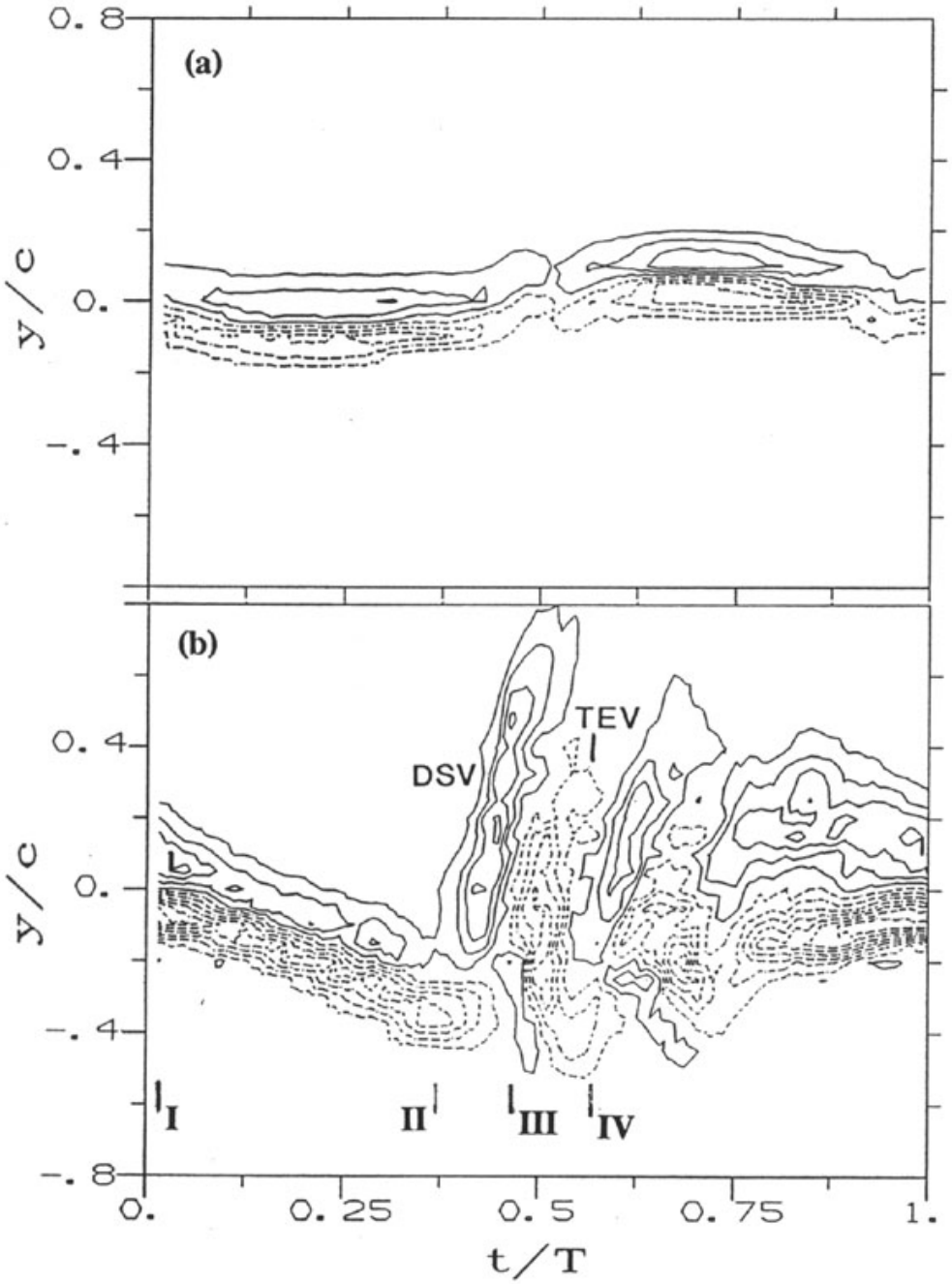

Fig. 9 Temporal distributions of $<\omega_z>c/U_\infty$ over a cycle, measured at x/c = 0.3; R_c = 44,000. Contour levels for positive vorticity (solid line) start at 0.5 and for negative vorticity (dashed line) at -.5 and are at an interval of 0.5. (a) $\alpha = 0° + 7.2°\sin 2\pi ft$, k = 0.028, (b) $\alpha = 15.3° + 9.7°\sin(2\pi ft - \pi/2)$, k = 0.16.

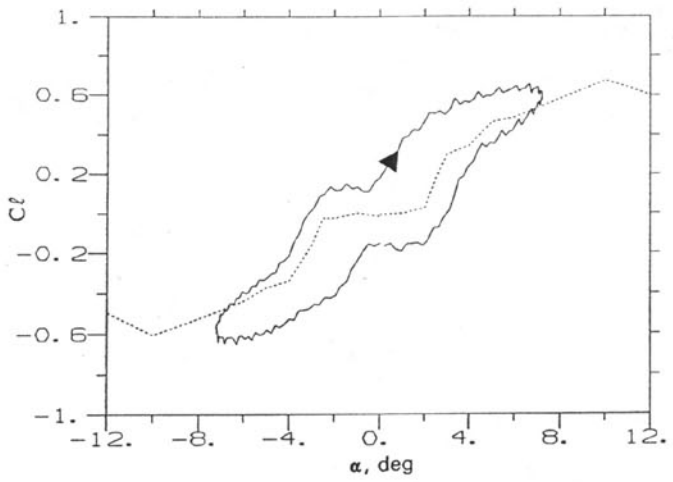

Fig. 10 $C\ell$ vs. α measured with a force balance for the case of figures 9(a): $\alpha = 0° + 7.2°\sin 2\pi ft$, $k = 0.028$. Dashed line represents steady state variation of $C\ell$ with α.

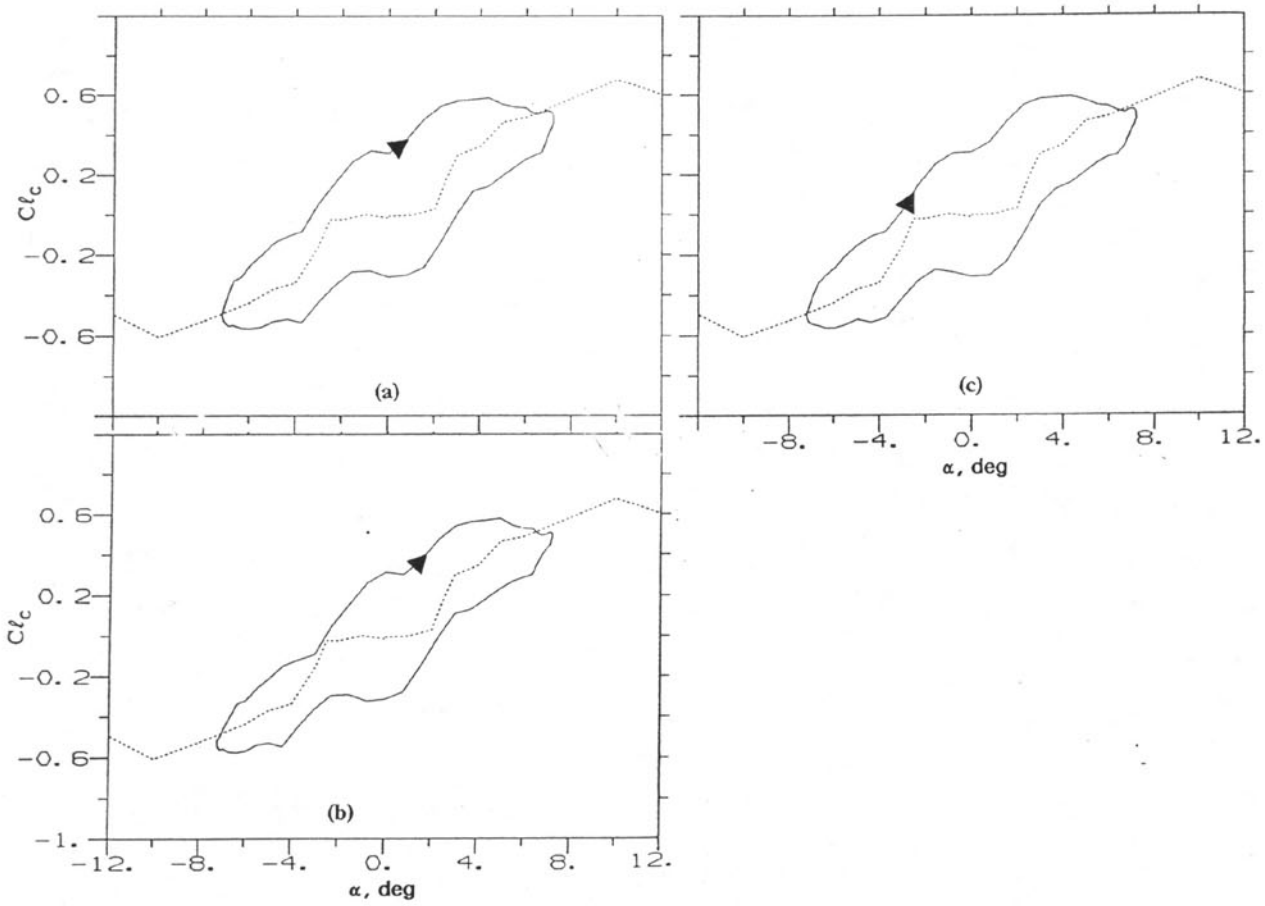

Fig. 11 Estimated $C\ell_c$ vs. α from the data of figure 9(a); $\alpha = 0° + 7.2°\sin 2\pi ft$, $k = 0.028$. (a) to (c) obtained using equations 1 to 3 (see text), respectively.

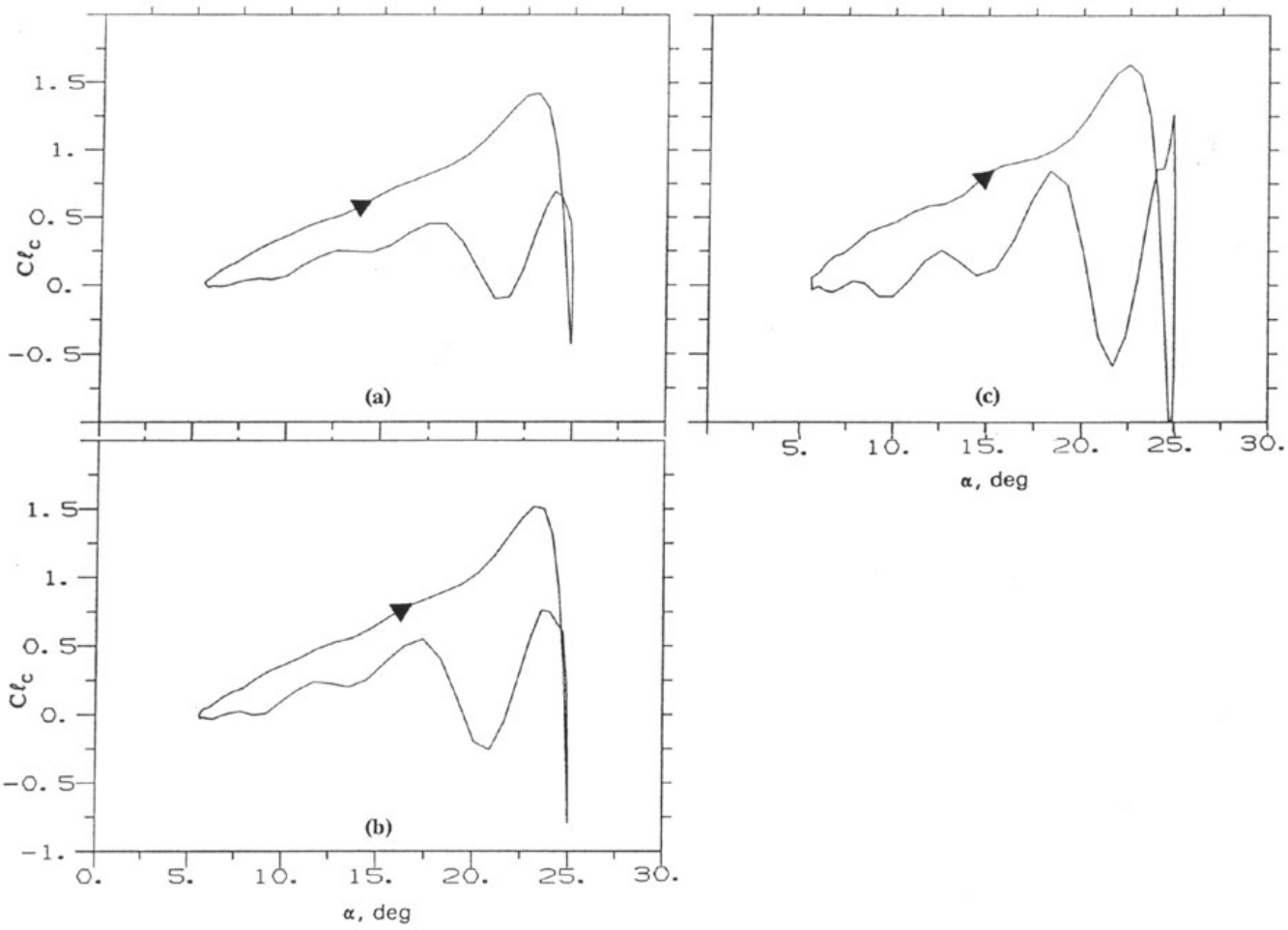

Fig. 12 Estimated $C\ell_c$ vs. α from the data of figure 9(b); $\alpha = 15.3° + 9.7°\sin(2\pi ft - \pi/2)$, $k = 0.16$. (a) to (c) obtained using equations 1 to 3 (see text), respectively.

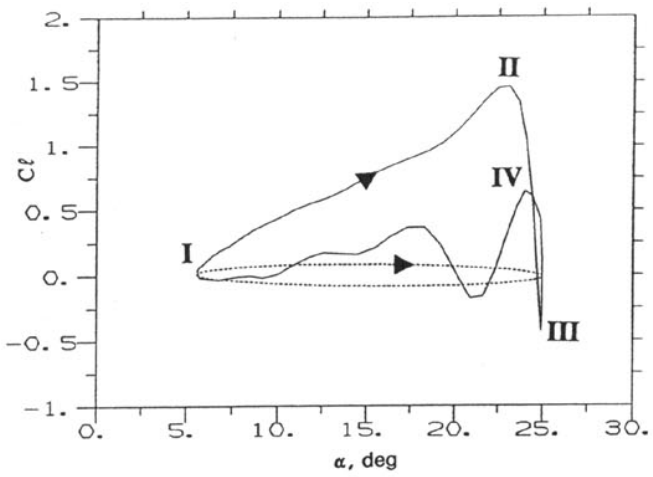

Fig. 13 Estimated, unsteady component of $C\ell$ vs. α obtained by adding the results of equation 1 (figure 12a) and the 'non-circulatory' component. The latter is represented by the dashed curve. $k = 0.16$, $R_c = 44{,}000$, $M = .019$.

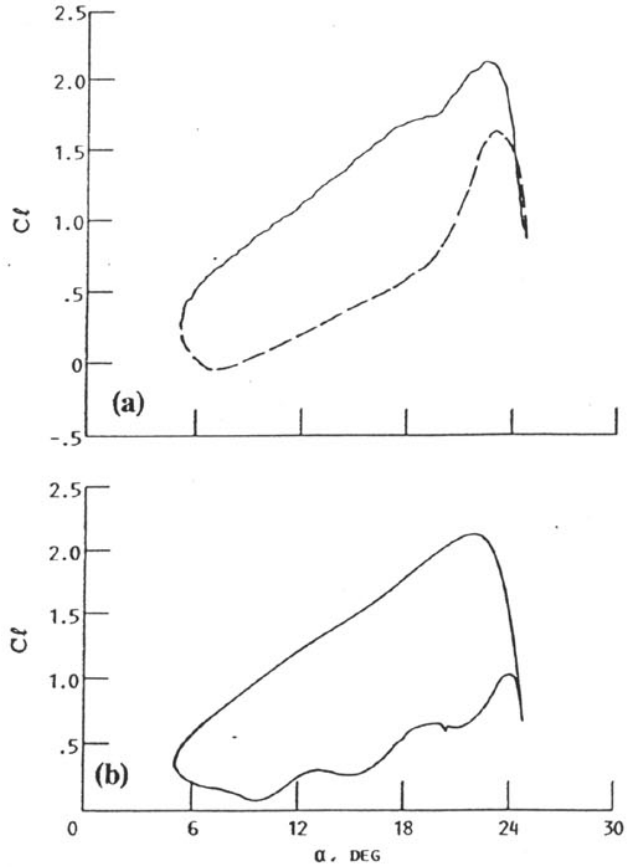

Fig. 14 Total $C\ell$ variation with α for $k = 0.153$, $\alpha = 15° + 10°\sin 2\pi ft$: (a) Experimental data of McAlister et al. (1982), $R_c = 4.8 \times 10^5$, Mach number, $M = 0.036$; (b) Computational data of L. N. Sankar (see Wu, Huff and Sankar 1990), $R_c = 3.45 \times 10^6$, $M = 0.283$.

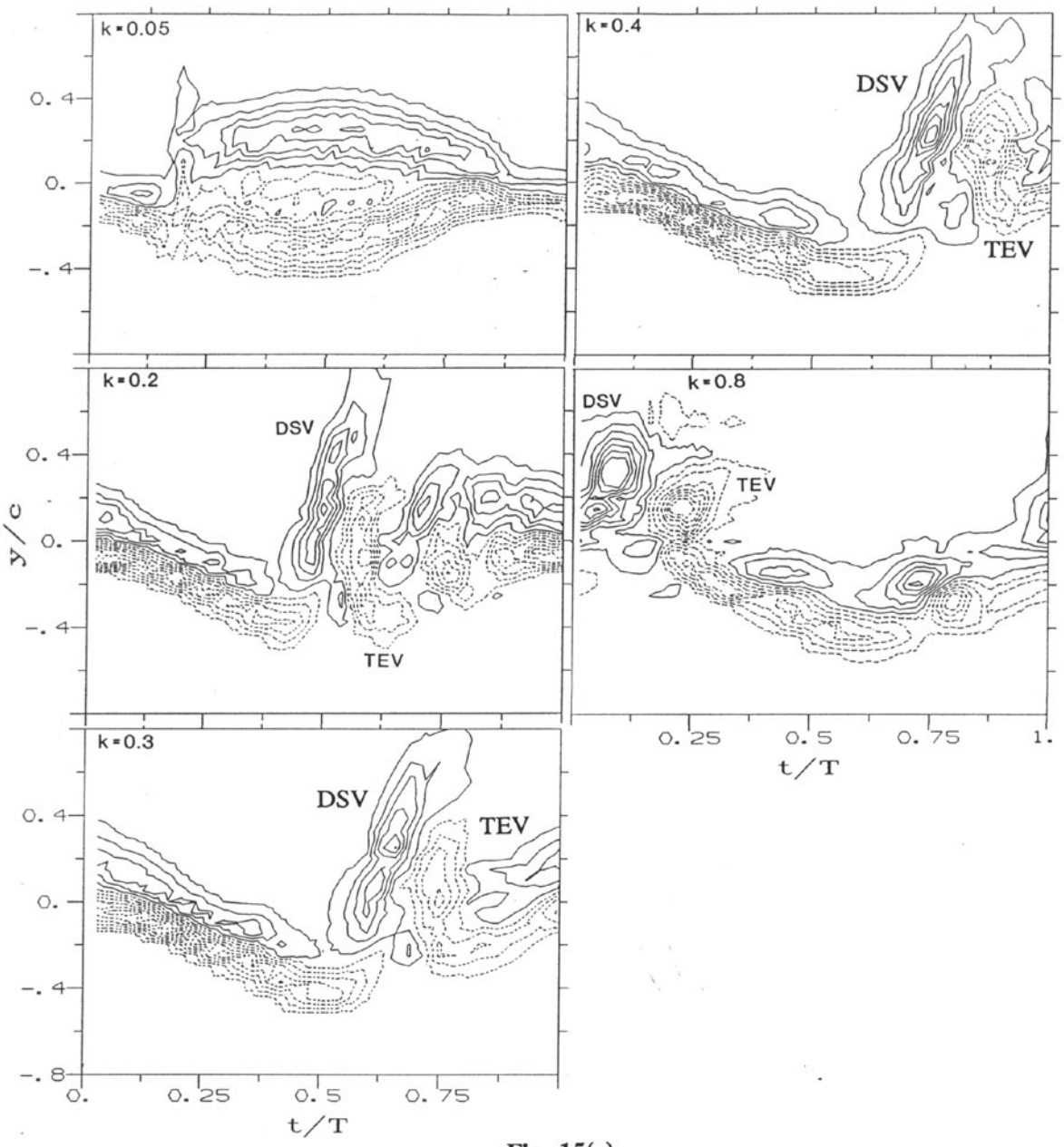
k=0.05
k=0.4
DSV
TEV
k=0.2
DSV
TEV
k=0.8
DSV
TEV
k=0.3
DSV
TEV
0.4
0.
-.4
-.8
y/c
0.
0.25
0.5
0.75
1.
t/T

Fig. 15(a)

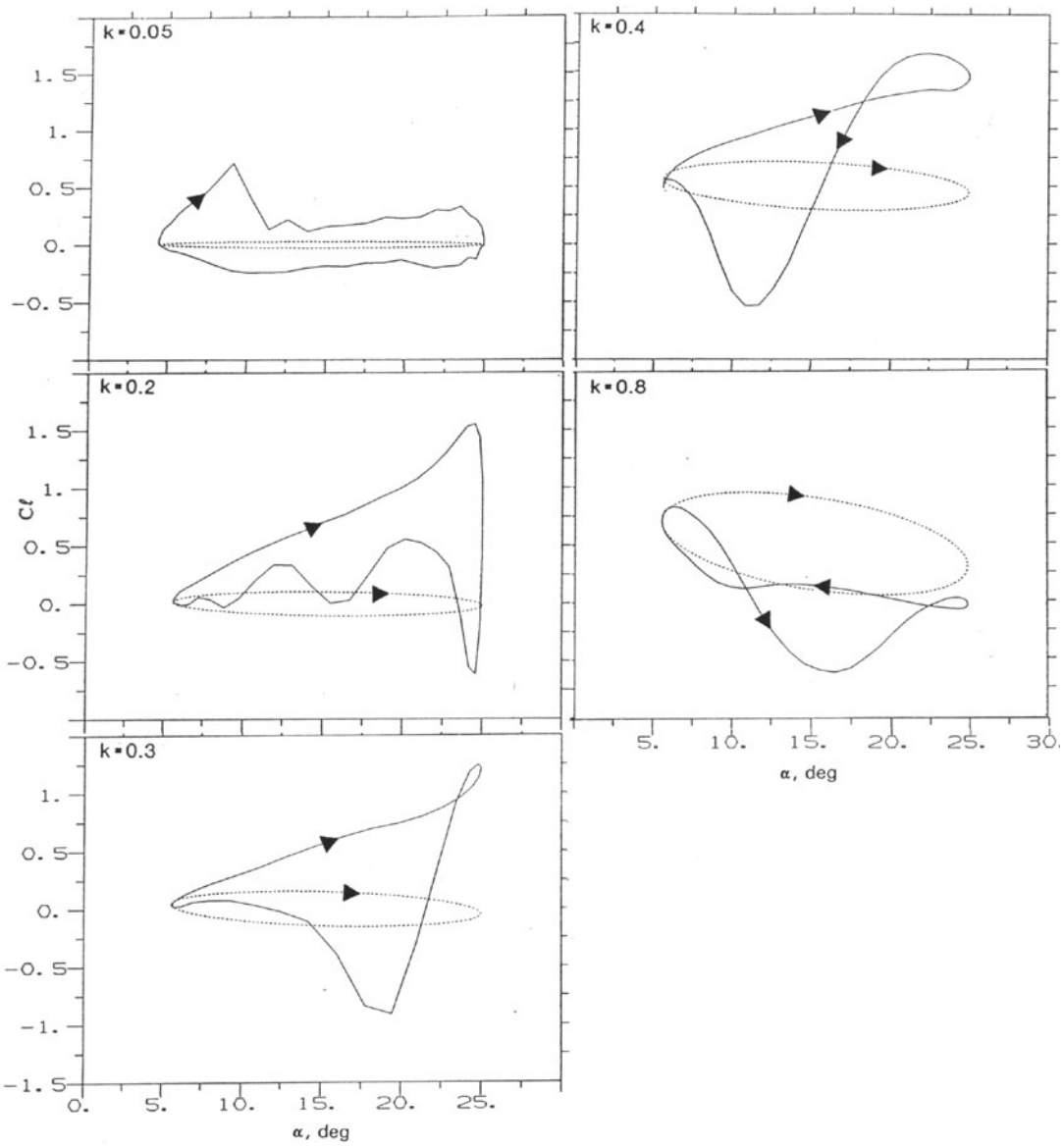

Fig. 15(b)

Fig. 15 Effect of k for $\alpha = 15.3° + 9.7°\sin(2\pi ft-\pi/2)$; $R_c = 44{,}000$ for $k = 0.05$ to 0.4 and $R_c = 22{,}000$ for $k = 0.8$. (a) $<\omega_z>c/U_\infty$ contours similar to the data of figure 9. (b) Estimated unsteady component of $C\ell$ vs. α; dashed curves represent non-circulatory component.

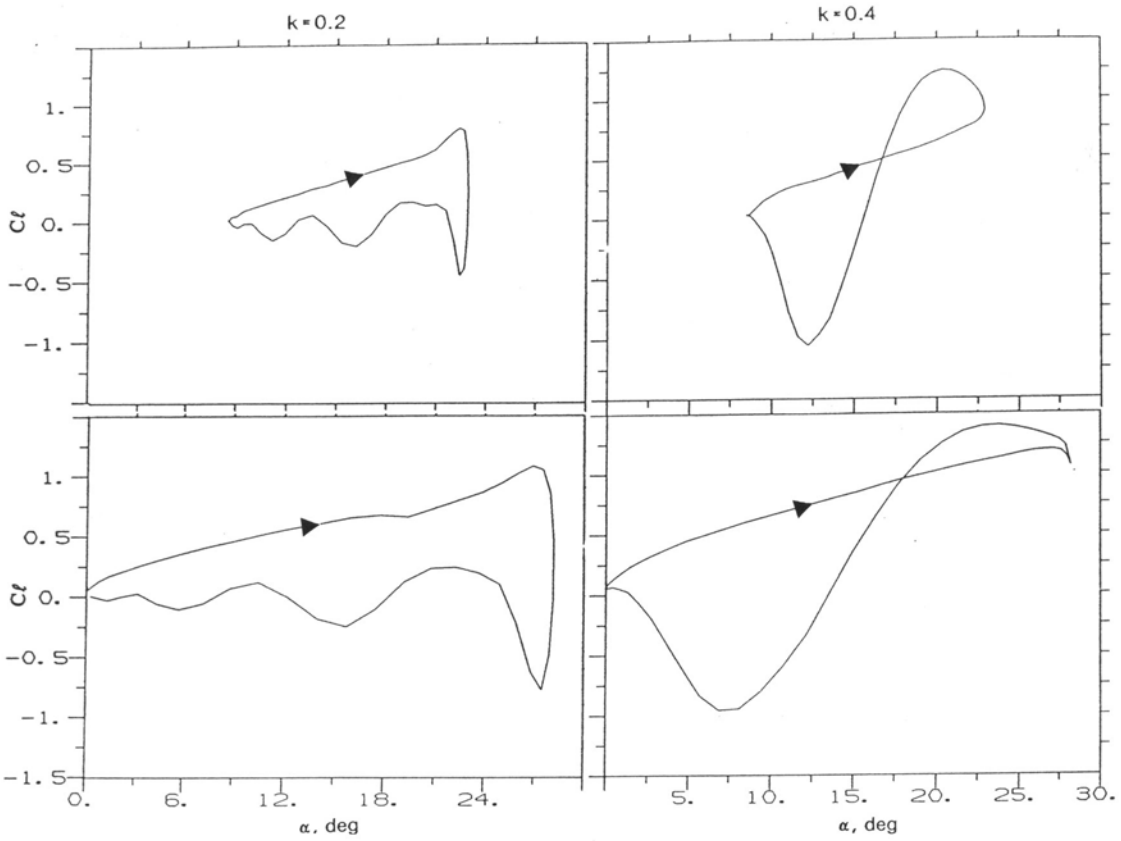

Fig. 16 Estimated $C\ell$ vs. α for two different amplitudes of oscillation for indicated values of k. Top row: $\alpha = 15.7° + 7.2°\sin(2\pi ft-\pi/2)$; Bottom row: $\alpha = 14.1° + 14.1°\sin(-2\pi ft-\pi/2)$.